Interface Electronics for Ultrasonic Transducers

by

Hao-Yen Tang

A dissertation submitted in partial satisfaction of the

requirements for the degree of

Doctor of Philosophy

in

Engineering - Electrical Engineering and Computer Sciences

in the

Graduate Division

of the

University of California, Berkeley

Committee in charge:

Professor Bernhard E. Boser, Chair
Professor David A. Horsley
Professor Liwei Lin

Spring 2016

Interface Electronics for Ultrasonic Transducers

Abstract

Interface Electronics for Ultrasonic Transducers

by

Hao-Yen Tang

Doctor of Philosophy in Engineering - Electrical Engineering and Computer Sciences

University of California, Berkeley

Professor Bernhard E. Boser, Chair

Ultrasound has long been used for medical imaging. Recent advances of miniaturized MEMS ultrasonic transducers new applications such as gesture recognition, personal fitness devices, and fingerprint sensors. These devices are considerably smaller than conventional transducers. To benefit from their lower excitation power requirements and address the reduced sensitivity requires the design of novel interface electronic circuits.

The first part of this thesis describes new circuits capable of generating all the high voltage drive signals for MEMS transducers on-chip from a single low-voltage supply. A novel level shifter design lowers power dissipation by suppressing the crow-bar current of conventional designs. The techniques have been verified in a seven channel ASIC and applied to a personal fitness application.

The second part of the thesis applies the new circuit ideas to the realization of an ultrasonic fingerprint sensor comprising over 6000 individual transducer elements in a 5x4 mm^2 area, each with drive and sense electronics. Unlike prevalent optical or capacitive fingerprint sensors, the ultrasonic solution is capable of recording both the surface and inner layers of the finger, resulting in reduced susceptibility to spoofing attacks.

To my grandfather: Tang, Shu-Yu.

Contents

List of Figures

Acknowledgments

"Wha..... I got the mail from UC Berkeley !? What the ( )...."

I'll never forget the day when I got the phone call from my father at the time when I was serving a compulsory military service in Taiwan. My father is a UC Berkeley EECS alumni under advising of Prof. Paul Grey. And thus UC berkeley has been my dream school for years.

And so, fig. 0.1 shows the one I want to acknowledge first: my adviser, Prof. Bernhard E. Boser. He's the one who gave me the chance to come to the US, to enter such a prestigious school, to meet so many talents people and to work on such an interesting project. Basically without him none of these will happen.

He's a really smart person, and he knows the trend of future technologies, which I think is the most important and valuable talent as a professor. At the very beginning when I don't know what to do, he told me to work on this ultrasonic fingerprint sensor project and said that: "This project will make huge impact!". I didn't think too much on it before, but as 4 years pass it proves that he's absolutely right: This project is exactly what industries want, and we've drawn A LOT of impacts on this project. Thanks to him I got the chance to experience what only a few Ph. D. students have: Witness your own project becomes a real product in industrious. I really appreciate him for all of these.

Nowadays if you want to do great work, very often you need to combine different techniques on different field. I'm so lucky that our groups have a very good collaborators: the

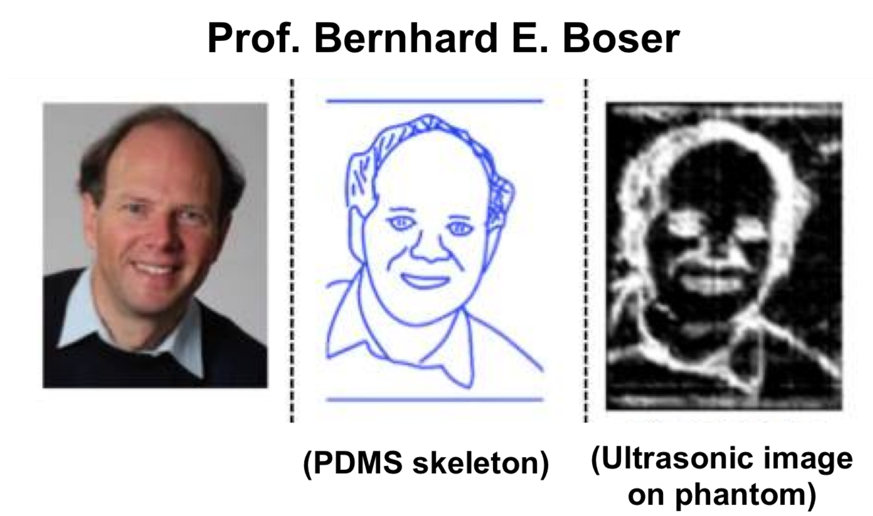

Figure 0.1: The "optical" image of my adviser, a skeleton drawing for making a PDMS phantom and an ultrasonic image taken for the PDMS phantom using the ultrasonic fingerprint sensor we developed.

MEMS team lead by Prof. Horsley shown in fig. 0.2. Although not officially my co-adviser, he also provided me valuable suggestions on MEMS to help me design better system. Getting one adviser in UC Berkeley is already my dream, but then I got 2! Without him and the work from his group, we couldn't achieve all those researches.

"Hey, big boss!" this is the "hello" for me to Dr. Richard Przybyla, the one who I worked with when I join the group. As a senior member of the group, he's so nice and teach me lots of things of acoustic, PMUT, circuit, etc. We together tape-out a chip, fight all the way to late night and still stay in the lab for layout, witness the chip works successfully and become a real startup: Chirp Microsystems®. I'll never forget those days.

As an international student as well as a bad English speaker, writing a paper is always a pain on the neck for me (and for the Prof. in fig. 0.1). I got a very good friend, Dongjin Seo, to help me a lot on this, but not only on paper writing. We've established good collaboration between our group and Prof. Maharbiz's group. Our ASIC was used in their project, and I'll be really happy to see our research spread out and make more impacts on different fields!

No sensor system could be built without sensor. I want to thank Dr. Yipeng Lu who made the transducers on our fingerprint sensors.

And I also want to mention, I have great lab-mates. We help each-other on difficult days, we celebrates together if someone's chip works or get an ISSCC, we discussed technical issues on designs – we stand together. I want to thank Yu-Ching Yeh, Dr. Pramod Murali, Behnam Behroozpour, Burak Eminoglu, Efthymios Papageorgiou, Joshua Kay, Luya Zhang and Sidney Buchbinder.

Finally, I want to thank my grandmom and parents. Both my parents work, so my

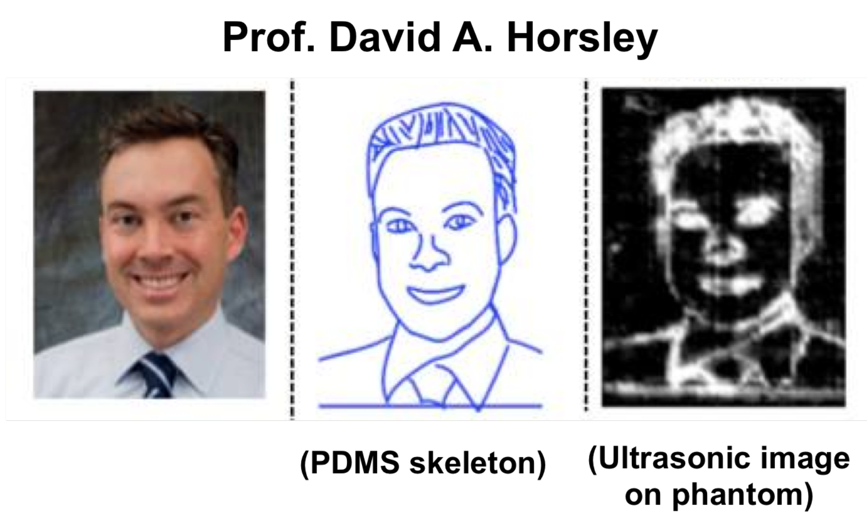

Figure 0.2: The "optical" image of Prof. Horsley, a skeleton drawing for making a PDMS phantom and an ultrasonic image taken for the PDMS phantom using the ultrasonic fingerprint sensor we developed.

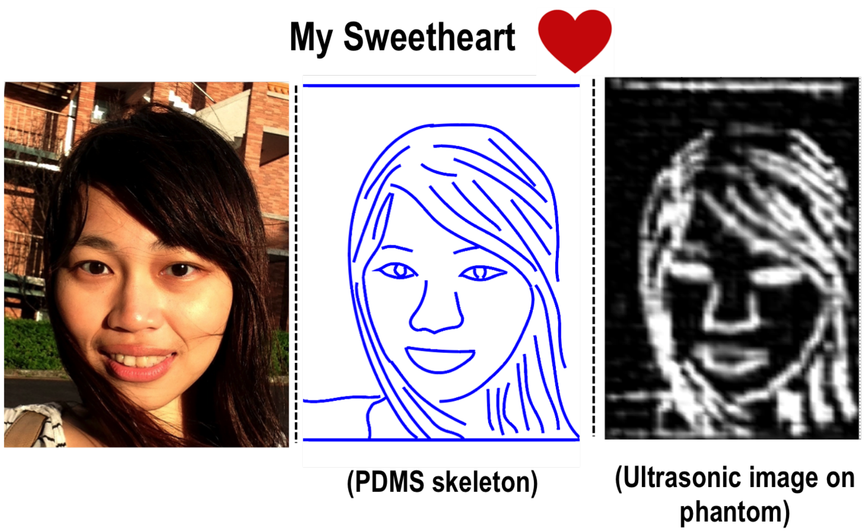

Figure 0.3: The "optical" image of my wife, a skeleton drawing for making a PDMS phantom and an ultrasonic image taken for the PDMS phantom using the ultrasonic fingerprint sensor we developed.

grandmom Liu, Qiu-Ju take cares of me when I was a child. My father, Tang, Yuan-Sheng, is a role-model for me (cmon, UC Berkeley alumni!) such that I could keep working hard on it to pursue him. My mother, Yang, Ling-Chu is always my mental support. Not only she raise me up with love and patient, but also she give me another power of working hard: I want to become successful and let her happy and proud of me.

"Even a blind chipmunk finds a nut in the woods every once in awhile", and I am so fortunate to have found Wei-Tzu Lin, my sweetheart (Fig. **??**. When I was happy I could share my joy with her, and when I was sad she could be my worry partner. The long-distance relationship due to my Ph. D. studies didn't weaken but further strengthen our love and finally lead to our marriage. I thank her for her love and accompanies, and I look forward to our next adventure.

Chapter 1

Introduction

Ultrasound is a powerful tool for non-invasive imaging and has a decades-long track record in medical imaging. Blood flow, anatomy, and stiffness of body tissue can be quickly computed from time-of-flight ultrasound echoes. Affordable miniature ultrasound systems can bring these benefits to a broader audience for example through tele-medicine and enable new applications such as fitness tracking or even enable 3D imaging of fingertips for robust and spoof-proof fingerprint verification.

Present electronic interfaces optimized for macro-scale transducers are capable of very high voltages and high power delivery, requirements not needed by novel miniature MEMS transducers. Optimizing electronics for these latter devices enables significant reduction of power dissipation, size, and cost.

The thesis is organized as follows. Chapter 2 describes the physics of ultrasound imaging including beam spreading and path loss. Chapter 3 describes a custom ASIC capable generating the phased-array driving signals for MEMS transducers. The circuit generates high-voltage drive signals up to 30-V on-chip from a 1.8 V supply. In Chapter 4, an application of the interface ASIC to a personal fitness device is described. This device measures the thickness of fat and muscle layers, apprising the user of the benefits (or lack thereof) of a fitness regime. The fully integrated ultrasonic fingerprint sensor described in Chapter 5 leverages the ideas presented in prior chapters. Although ultrasonic fingerprint sensors [1] have been available commercially for a while, conventional solutions use macro-transducers and mechanical scanning, features that render them both too large and too costly for integration in smartphones and upcoming IoT applications. The greater robustness of the ultrasonic solution compared to existing capacitive and optical devices make it an attractive candidate for next generation fingerprint sensors. Chapter 6 concludes the thesis.

Chapter 2

Challenges of Current Ultrasonic Imaging System

In this chapter, we first introduce the basic physics of acoustic, and then we describe the main drawbacks of ultrasound transducers and the dependency on high-voltage driving. Followed by an example block diagram of the current ultrasonic imaging system, the chapter concludes with a lists of problems that prevents an ultrasonic imager system from miniaturizing.

2.1 Basic Acoustic Physics

Typically, an ultrasonic transducer utilizes piezoelectric effect when driven with voltage to deform and generate acoustic waves to propagate in a media. Typically, the transducer is driven at its resonance frequency to maximize the transmit efficiency, $\eta_{TX} = P_{TX}/V_{TX}$, where P_{TX} is the output pressure amplitude and V_{TX} is the driving voltage. The beam-pattern of the generated wave is mainly determined by the size and the frequency of the transducer.

In addition to pressure, acoustic waves transmitted to a media are described by velocity, acoustic impedance and volume velocity. Shown in Fig. 2.1, P and v represent the pressure and velocity (speed of sound) of the wave, respectively. In any media, the ratio P/v is constant and is defined as the *acoustic impedance* Z_a of the media with the unit *Rayl* or Pascal second per meter ($Pa \cdot s/m$). The *Volume velocity* $V_v = v \times A$ where A is the cross-sectional vector area represents the average wave velocity at the cross-section A. The product $P \times V_v$ has the unit of *Watt*. With this notation, P and V_v resemble the voltage and current in electronics, and the media can be modeled as a transmission line with characteristic impedance $Z = Z_a/A$.

As the wave transmits in the media, it loses intensity due to both *attenuation* L_{att} and *beam spreading loss* L_{sp} [2]. The attenuation is the result of the thermo-viscous heating of the media molecules along the path and can be modeled as $L_{att}(d) = e^{-\alpha d}$ where d is the

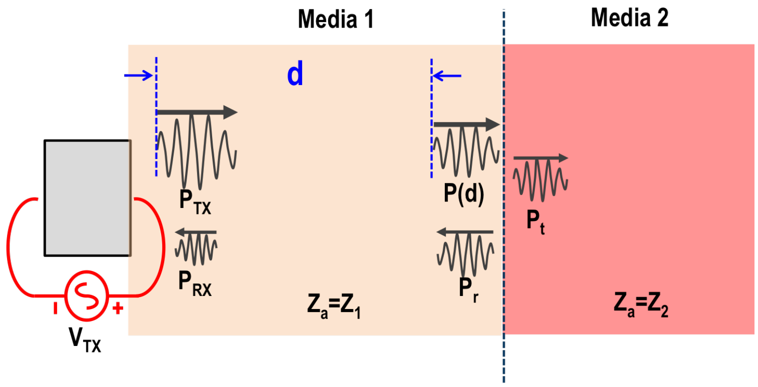

Figure 2.1: Propagation of ultrasonic waves and reflections at the interface between media with different acoustic impedances.

propagation distance and α is the attenuation coefficient. Beam spreading is described by $L_{sp}(d) = \sqrt{C/d^n}$ where C is a constant and n is a number between $1 \sim 2$, with 2 being the spreading loss for an ideal, omni-directional point source. Assuming the pressure spread out evenly from the transducer area A_m to a hemi-sphere with radius d, the spreading loss could be further written as $L_{sp}(d) = \sqrt{A_m}/\left(4\sqrt{\pi}d\right)$. This equation implies that the energy generates from the transducer is evenly distributed to the sphere. Consequently, the wave pressure after traveling a distance d is: $P(d) = P_{TX}L_{att}(d)L_{sp}(d)$.

Similar to transmission line theory, part of the wave hitting the boundary between two different medias with different acoustic impedance Z_a will be reflected as shown in Fig. 2.1. Since the wave area A is same at the boundary, the reflection index $\Gamma(d) = P_r/P(d)$ can be expressed as $\Gamma = (Z_2 - Z_1)/(Z_2 + Z_1)$. The transmission index $T = P_t/P(d)$ equals $1 + \Gamma$. The reflected wave then travels back towards the transducer suffering additional attenuation L_{att} and L_{sp} and is picked up by the same transducer where it results in a voltage $V_{RX} = \eta_{RX} \cdot P_{RX}$. The round-trip efficiency (V_{RX}/V_{TX}) for an ultrasonic transducer is usually less than 1% even without any acoustic loss.

2.2 Path-Loss Calculation Example

With the background described above, we then use an example modeling an ultrasound imaging for human abdomen to explain the link budget and then the need of high-voltage driving of ultrasonic transducers.

Figure 2.2 shows an acoustic model of the abdomen with the abdominal muscle sandwiched between subcutaneous and visceral fat layers. For fitness assessment, the thickness of the subcutaneous fat layer and the abdominal muscle are of primary interest and typically are at less than 5 cm depth. The system must therefore be capable of imaging to depth of at least 5 cm with 1-2 mm resolution. The acoustic reflection coefficient between fat and muscle

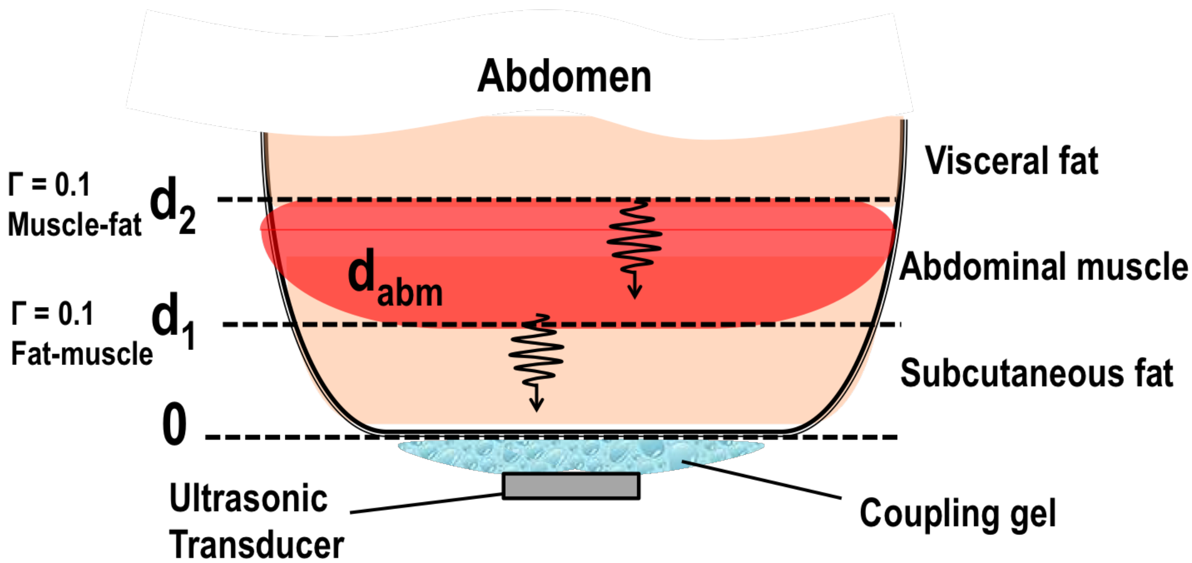

Figure 2.2: Acoustic model of the abdomen.

is approximately $\Gamma_m = 0.1$ [3, chapter3]. A PDMS layer and coupling gel are used between the transducer and the skin to achieve near perfect transmission of the ultrasonic signal.

We use a commercial PZT film transducer as our example device for calculation. The transducer consists a PTZ film with $d_{33} = 400\,\mathrm{pm/V}$ and $800\,\mu\mathrm{m}$ thickness. The device used in the experiments reported here consists of seven identical stripes of 1.4 mm width and 10 mm length and total area $A_x = 1\,\mathrm{cm}^2$ [4]. The device is operated at its resonant frequency $f_o = 2\,\mathrm{MHz}$ and the bandwidth is 400 kHz, resulting in 1.9 mm depth resolution in water. Tissue has very similar acoustic properties.

The transmit and receive efficiencies are $\eta_t = 2\pi f_o d_{33} Z_{\mathrm{H2O}} = 38\,\mathrm{kPa/V}$ and $\eta_r = 225\,\mathrm{nV/Pa}$ (measured), corresponding to $\eta_t \eta_r = -41\,\mathrm{dB}$ attenuation. At $d = 5\,\mathrm{cm}$ distance the spreading loss is $\sqrt{A_m}/\left(4\sqrt{\pi}d\right) = -31\,\mathrm{dB}$. The loss in tissue is -2.4 dB/cm or -12 dB at 5 cm [5]. The overall loss, including transducer, spreading, and tissue at 5 cm adds up to -104 dB.

Fig. 2.3 shows the signal-to-noise ratio assuming a typical $30\mu V$ integrated noise at receiver and the equation that shows all the parameters of the link budget. The figure suggests that with the loss of -104 dB, even to reach 0dB of SNR the driving voltage V_T needs to be as high as 12V. In reality, a greater driving voltage is even needed to achieve enough signal-to-noise ratio. This shows the need of high voltage driving in ultrasonic imager system due to significant path loss along with poor conversion efficiency of ultrasonic transducers.

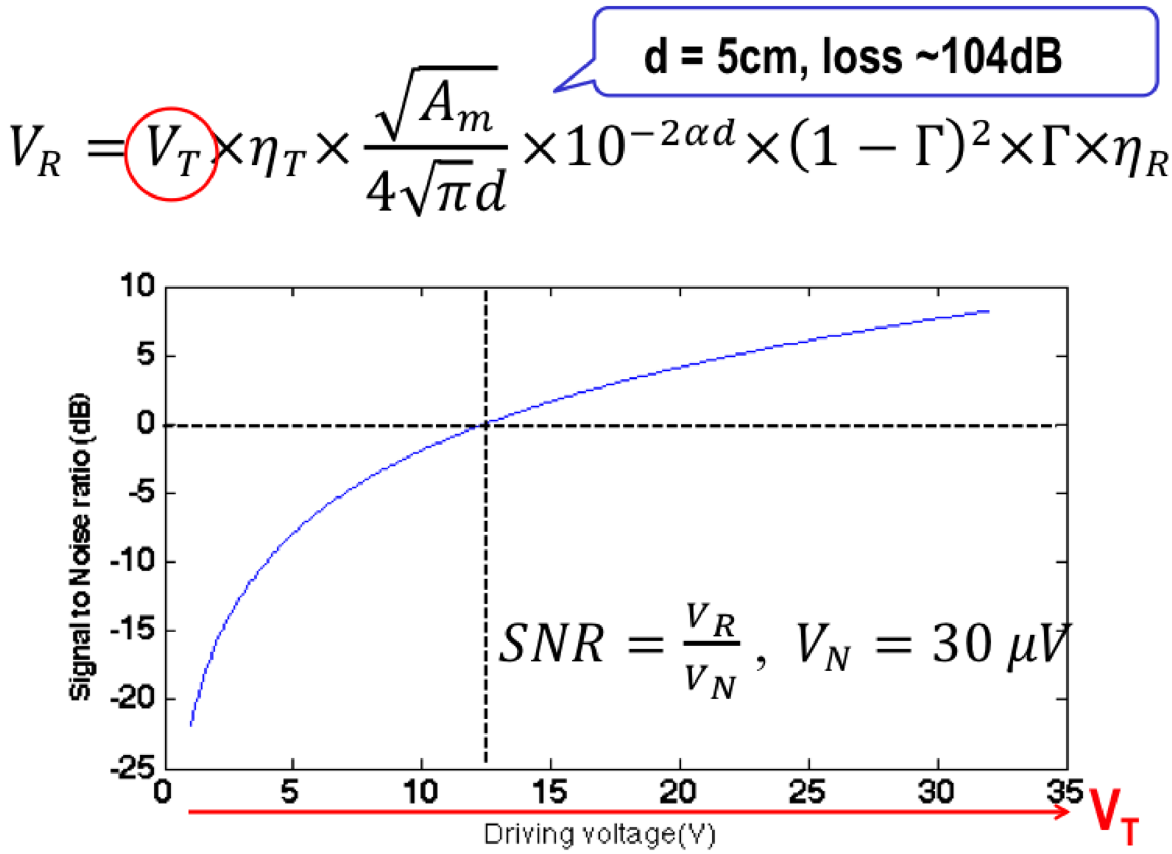

Figure 2.3: Typical SNR v.s. driving voltage with a commercial transducer.

2.3 Drawbacks of Current Ultrasonic Imagers

Fig. 2.4 shows a typical system block diagram of a medical ultrasonic imager. On the transmit (TX) side, a combination of a beamforming chip, a high-voltage (HV) pulser, and high-voltage supplies are used to drive a transducer array. On the receive (RX) side, a dedicated front-end circuit with high-voltage isolation switches to prevent any TX feedthrough, preamplifiers, and ADCs are used to amplify and digitize the data for digital processing of the received echoes.

The majority of efforts to miniature ultrasound systems have focused on transducer arrays and the readout electronics. Recent progress in the micromachined ultrasonic transducers (MUT), including capacitive MUTs [6] and piezoelectric MUTs [7], significantly reduced the power consumption and the process variations in the assembly of 2-D MUT arrays by miniaturizing transducers and optimizing the fabrication process [8]. Furthermore, advancements in the wafer bonding processes [9], [10] have enabled heterogeneous integration of CMOS and MUT wafers, which further miniaturizes and improves the power efficiency of the system by

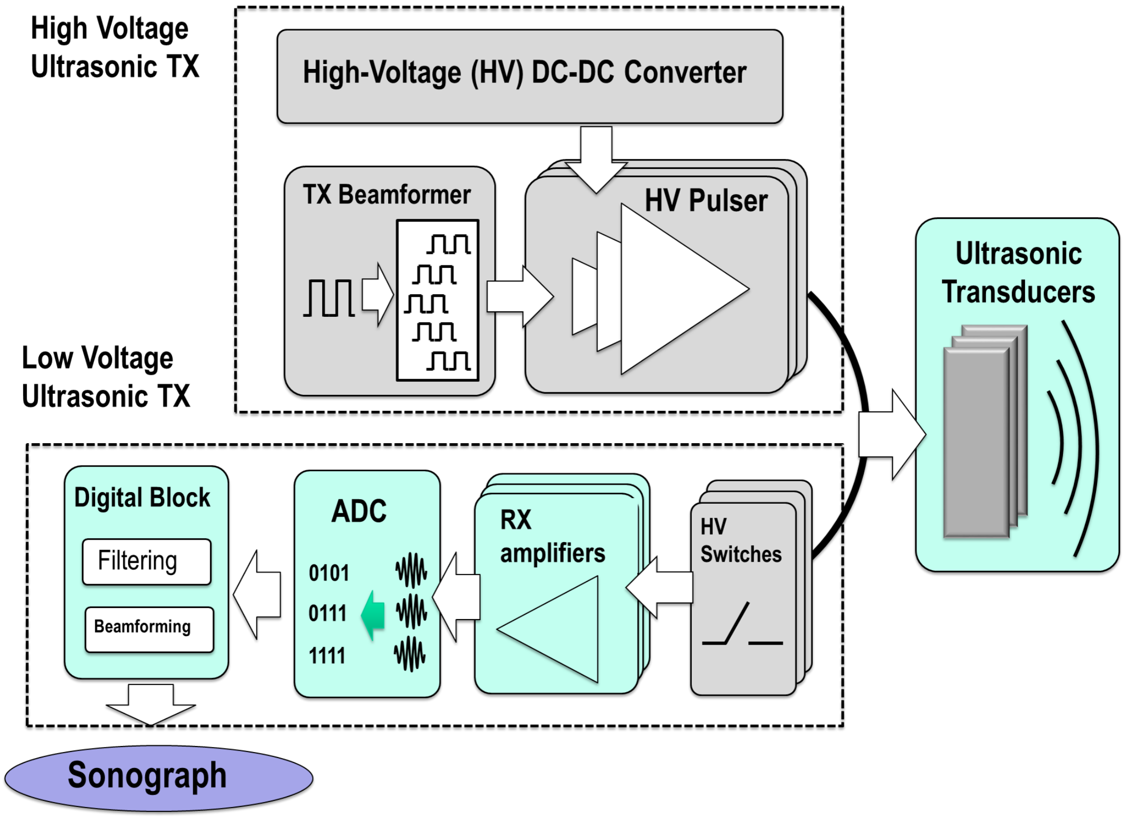

Figure 2.4: System diagram of an ultrasonic imager

reducing the interconnects and the associated parasitics. Together with the advances in the bonding process, recent reports on circuit techniques for ultrasonic receiver and data processing have demonstrated integrated ultrasonic systems for real-time ultrasonic imaging [11], over-the-air gesture recognition [12], finger-print detection [13], and many more [14].

However, the necessities of high-voltage electronics significantly increase the system complexity of ultrasonic imager system. In order to meet the cost and size constraints of portable consumer devices, high-voltage supplies need be integrated. In addition, drivers for the transducer array must be properly designed to prevent any leakage or static power consumption from high-voltage supplies to meet the power constraints. Current commercially available ultrasonic TX module [15], however, requires several external power supplies, up to ± 50 V, and consumes close to 4.5 W of instantaneous power when driving an 80 pF load at 5 MHz. Although the average power consumption of the TX can be low for a heavily-duty cycled system, local heating spots generated from the excessive power consumption of the electronics present safety concerns, especially when interfacing with the human body [16]. As a result, there has been a number of papers focusing on improving the driver efficiency [11], [17] – [19]. However, these designs still require external high-voltage supplies and implement traditional latch architectures that are large and slow. In short, despite the progress on transducers and receiving side, the high-voltage supply and driver circuitry remains unsolved issues that prevents the system from miniaturizing.

2.4 Summary of the problems on current ultrasonic imagers

In summary, current ultrasonic imagers have several drawbacks:

Low conversion efficiency The poor conversion efficiency η_T and η_R of ultrasonic transducers significantly increase link budget.

Significant path-loss The attenuation and spreading loss greatly reduce the signal after transmission.

High-voltage dependency To compensate for the high path loss, ultrasonic transducers are usually driven with high-voltage pulses which greatly increase the system complexity.

The high-voltage needed in the current system also results in the following problem:

Large off-chip passive components To implement high-voltage supplies, passive components such as a transformer or inductors are desired, which is too bulky to be built on chips.

Power consumption The lack of efficient high voltage driver circuit makes the system power hungry. Although this is not a big consideration in medical devices, it prevents the imagers to be implemented on consumer electronics.

Interface with low voltage devices Typically a standard CMOS process is much favorable for front-end electronics for its better efficiency and noise performance comparing to high-voltage transistors. However, they need to be protected from high-voltage pulses, and thus the interface between HV-TX, RX, and transducers becomes complex.

Finally, in ultrasonic system contains an array of transducers, accessing to individual pixels becomes a big issue. For example, in the ultrasonic fingerprint sensor design proposed in this dissertation, over 6000 pixels are needed to successfully image a 4.73 by 3.24 mm^2 fingerprint.

In the rest of this dissertation, we'll propose the solution to all the problem above, and finally leads to a miniaturized ultrasonic imaging system that could be incorporated into consumer electronics.

Chapter 3

Single 1.8V-Supply Ultrasonic Interface ASIC Design

This chapter describes an ASIC that addresses some of the limitations outlined in the previous chapter including

An on-chip 1.8 V to 32 V voltage booster,

A low-power and high speed level shifter,

A beamforming transmitter and

A high-voltage receive-transmit switch with low parasitics.

3.1 Chip Architecture

The ASIC [20] essentially integrates all the blocks labeled with grey color in Fig. 2.4 with one chip which serves as a complete, fully-integrated 7-channel ultrasonic imager that consists of high-voltage ultrasonic TX, including TX beamformer, HV driver, and on-chip HV DC-DC converters, as well as RX front-end with isolation switches and preamplifiers. An on-chip charge-pump generates all necessary high-voltages supplies on-chip from a single 1.8 V external supply, enabling a compact and low power solution.

Fig. 3.1 shows the block diagram of an system consisting of the ASIC , a piezoelectric transducer array, and to reduce the system complexity, data conditioning and processing done with FPGA, off-chip ADCs, and buffer amplifiers with 0.1 MHz to 5 MHz bandpass filters. The entire system is powered by a single 1.8 V source. The ASIC has 7 identical channels, each consisting of TX beamformer with 6-bit delay control with 5 ns resolution, HV level-shifters, HV DC-DC converters, and HV TX/RX switches that isolate the RX front-end from the high TX voltage. All necessary high-voltage levels are generated with

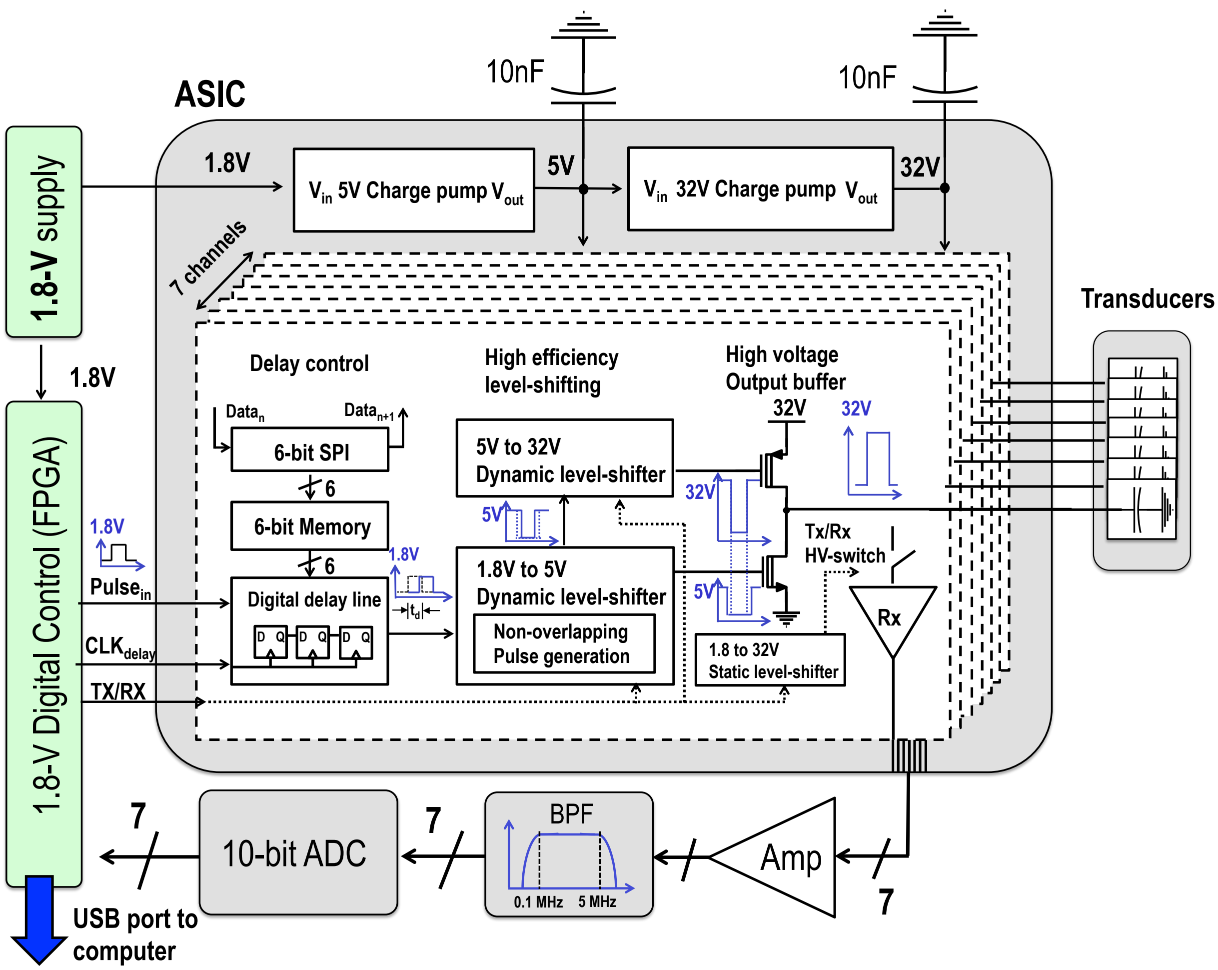

Figure 3.1: System architecture of the proposed single-supply ultrasonic imager.

on-chip 5 V and 32 V charge pumps from the 1.8 V supply. Two 10 nF off-chip capacitors are used to regulate the charge-pump output.

3.2 High-Voltage Level-Shifting

The TX level-shifter shifts the input pulses to the high voltage needed by the ultrasonic transducer. These level-shifters must operate at high frequencies and generate 32 V output under the power budget constrained by the on-chip charge pumps. This section describes the conventional level-shifter architectures and their limitations and our proposed design.

Static Level-Shifter

Fig. 3.2a shows an implementation of a latch-based level-shifter, which consists of an NMOS differential pair and a PMOS negative resistance load. Although simple, this circuit has several drawbacks. First, the NMOS transistors need to be large in order to overpower the PMOS load, which is driven with a much higher gate-to-source voltage due to the high-voltage supply. Enlarging the input NMOS pair results in high input capacitance, which limits the maximum operating speed and increases the power dissipation in the driver circuit. Second, although static, the circuit is subject to high dynamic power dissipation due to crow-bar current flowing during the transition when both the NMOS and PMOS transistors are conducting. Especially at the MHz operation typically used in medical ultrasound, crow-bar current dominates the overall power dissipation.

Several solutions have been proposed to overcome these shortcomings. The circuit in Fig. 3.2b employs degeneration in the NMOS devices to limit the maximum current to I_0 [21]. While this reduces the crow-bar current and hence improves the power efficiency, this solution further degrades the maximum operating speed.

The circuit in Fig. 3.2c avoids these drawbacks by separating the voltage step-up and the output driver [22]. The latter consists of NMOS and PMOS switches with non-overlapping control signals generated with a level-shifter similar to that in Fig. 3.2a, but with a cascode in series with the NMOS input pair. Biasing the cascode devices at approximately half the high-voltage supply reduces the PMOS overdrive voltage and hence the required NMOS pull-down strength. Although this solution can achieve a fast switching time, it requires a separate high-voltage supply, which is not desirable.

In this work, we propose a new architecture to suppress crow-bar current while simultaneously achieving high switching speed and low-power operation and avoiding the need for additional supplies.

Dynamic Level-Shifter: Concept

To overcome the power consumption due to crow-bar current, Fig. 3.3 shows the circuit proposed in this work. It retains the basic latch structure, but introduces additional high-voltage devices in series with the latching transistors. The timing diagram shows the signal waveform during the high-to-low transition of V_{o-}. As indicated by the dashed waveform, the switch $M_{\mathrm{sw}+}$ opens before the low-to-high transition of V_{i+} and closes after the output has settled. This effectively removes the pull-up $M_{\mathrm{p}+}$ from the output during the transition, thus enabling the use of a small NMOS pull-down $M_{\mathrm{n}+}$ with low input capacitance and permitting high speed operation. Opening $M_{\mathrm{sw}+}$ also prevents crow-bar current from flowing.

However, circuit implementations of the level-shifters in Fig. 3.3 have to overcome two challenges. First, in order to prevent crow-bar current, ideally, the rising edge of $V_{\mathrm{sw}+}$ needs to lead the rising edge of V_{i+}. In practice, however, it is not possible to predict when the

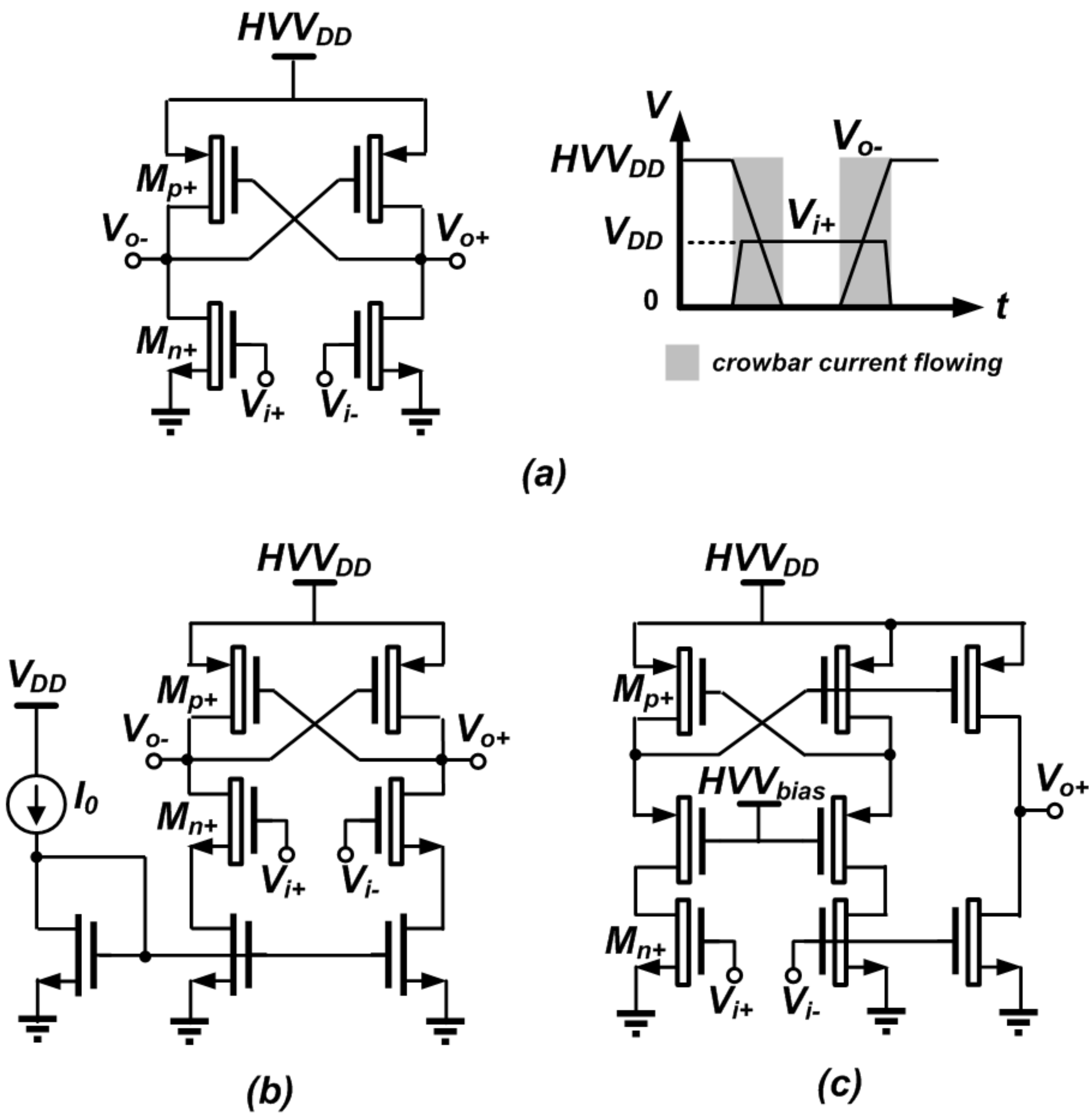

Figure 3.2: Level-shifter. (a) Conventional (b) Current limited (c) Voltage limited.

rising edge of the input will occur. Therefore, the solution adopted in this implementation, indicated by the solid trace, opens $M_{\mathrm{sw}+}$ after a fixed delay t_d after V_{i+} falls to prepare for the incoming high-to-low transition of V_{o-}, obviating the need for a control signal. The second challenge is that V_{sw+} and V_{sw-} are high-voltage signals, requiring a level-shifter and hence high voltage supply to properly control them. In a previous work [23] with a similar crow-bar current preventing switch, the switch is controlled by low-voltage V_{DD} signal which limits the upper-bound of HVV_{DD}. In our work, we accomplish high-voltage switch control by cross-coupling two high-speed level-shifters, as shown in Fig. 3.4, where each cell provides

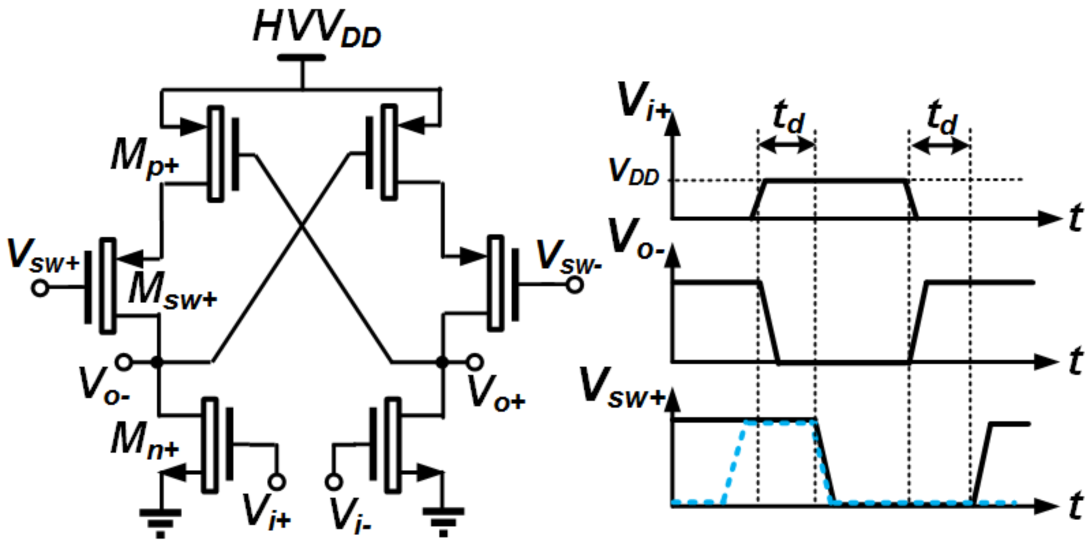

Figure 3.3: High-speed level-shifter with crow-bar current suppression.

high-voltage switch signals to the other.

Dynamic Level-Shifter: Complete Circuit

From the timing diagram in Fig. 3.3, it is evident that the switch control signals are simply delayed and inverted versions of the input signals and can therefore be generated with an identical level-shifter driven with a delayed input $V_{i,d}$. Fig. 3.4 shows the complete diagram consisting of two identical level-shifter cells. As indicated by the timing diagram in Fig. 3.5a, with the input $V_{i+,d}$ delayed by $t_d = \Delta T$, cell B provides the high-voltage output signal $V_{o+,d}$ and $V_{o-,d}$ to control cell A switches $M_{\text{sw}+}$ and $M_{\text{sw}-}$. On the other hand, for a square wave input with a period of T, the negative input of cell A, V_{i-} is also a delayed version of cell B input with $t_d = T/2 - \Delta T$. Hence, cell A outputs, V_{o-} and V_{o+}, are delayed versions of cell B outputs and thus can be used to control cell B switches. Finally, although functionally identical, cell A is sized larger to accommodate for differences in the output load.

Dynamic Level-Shifter: Idle Recharge

A potential problem with this circuit may occur when the output is not switching for a prolonged time, i.e., approximately 10 ms in this implementation. Consider the level-shifter cell in Fig. 3.4 where V_{o-} is high. The stacked PMOS and NMOS devices are then on and off, respectively. To prepare for the next cycle operation, the switch transistor, controlled by V_{sw+}, is on initially but turns off after a short delay, as illustrated in the idle timing diagram

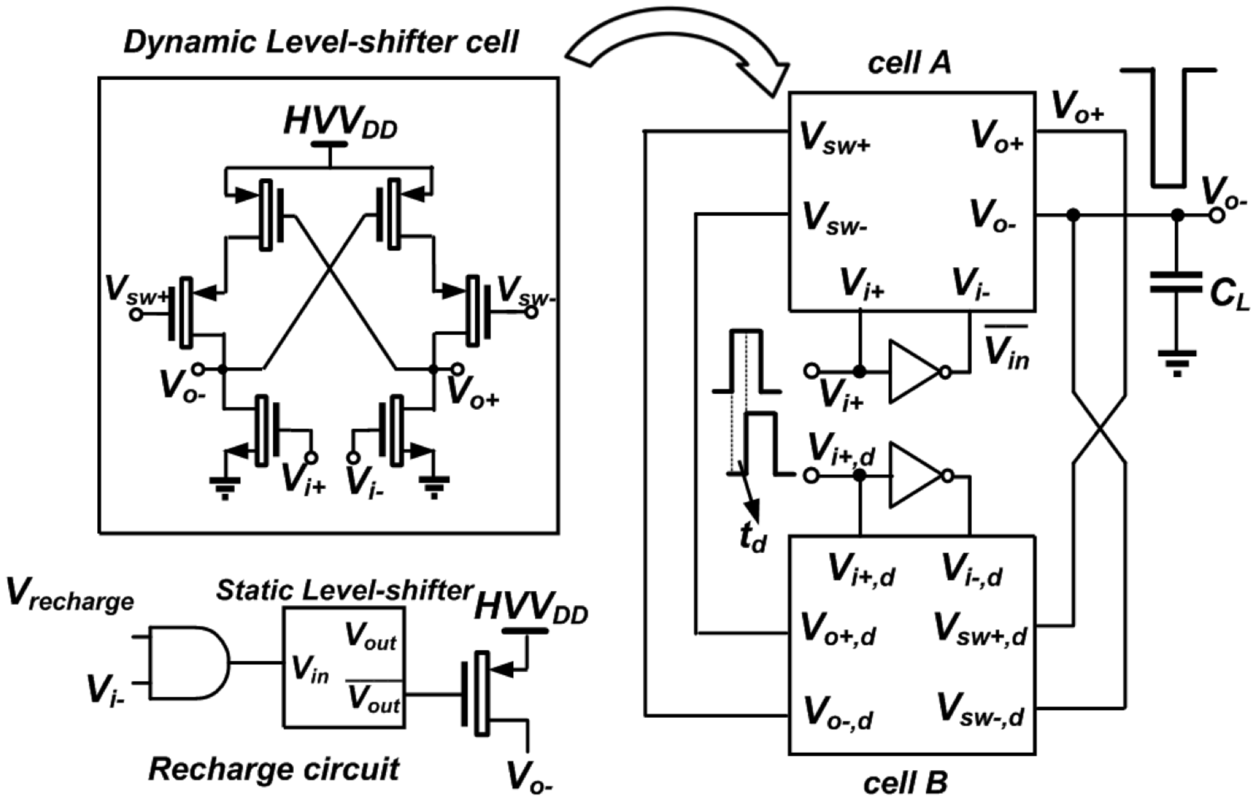

Figure 3.4: Complete architecture of the proposed dynamic level-shifters.

in Fig. 3.5b. At that point, V_{o-} becomes floating, eventually discharging completely. In applications requiring static operation, this situation must be avoided.

This problem can be circumvented by introducing a recharge circuit as shown in Fig. 3.4, consisting of a static level-shifter in Fig. 3.2a and a recharge signal $V_{recharge}$. As $V_{recharge}$ goes high, the circuit turns on HV-PMOS to recharge V_{o-} back to HVV_{DD} and vice versa for V_{o+}. Since $V_{o-,d}$, unlike V_{o-}, is always driven until V_{o+} changes state, there is no need to add recharge circuit to cell B. Additionally, unlike the core circuit, the requirements on the operating speed of the recharge circuit is low, enabling its implementation with smaller transistors to reduce power consumption and loading for the core circuit. In this work, $V_{recharge}$ is generated off-chip with an FPGA to indicate a lack of activity in V_{i+}.

3.3 Detailed Circuit Diagram

Driver Chain

The proposed level-shifter achieves both high-speed and low-power but cannot drive large capacitive loads and must therefore be buffered. A simple static CMOS inverter would suffer

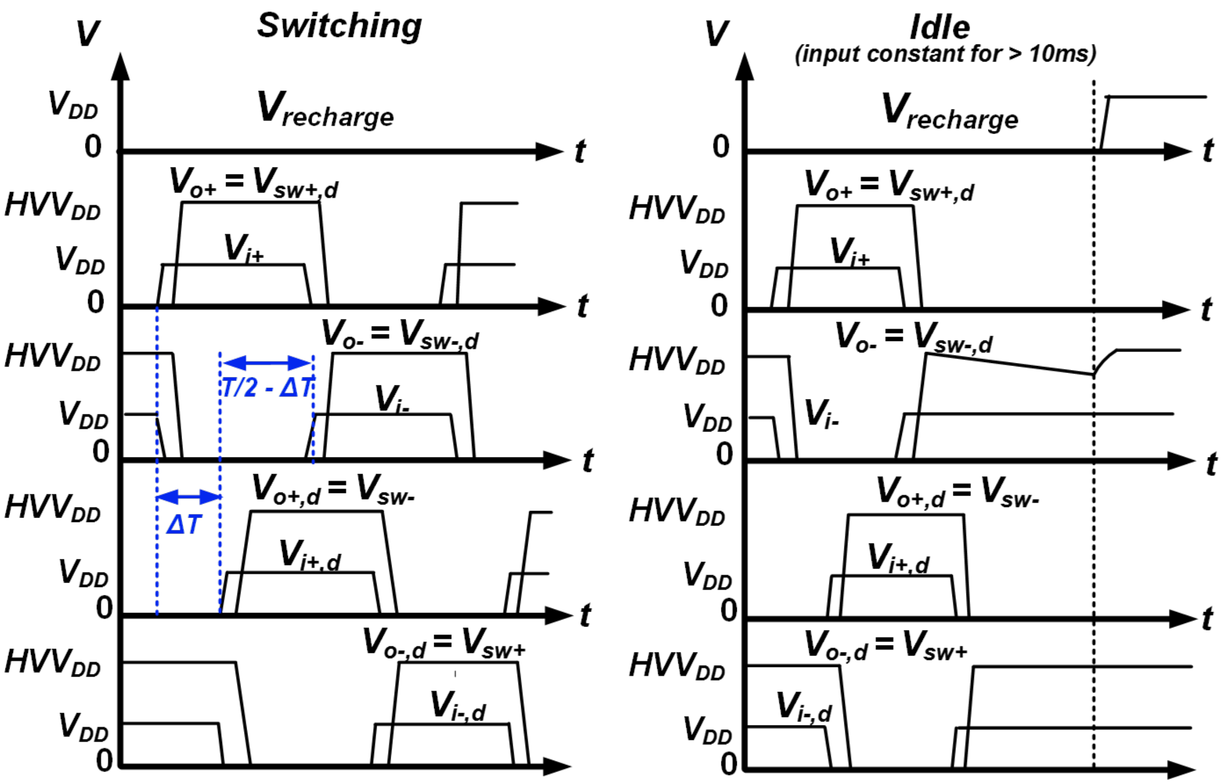

Figure 3.5: Output waveform during (a) switching (b) idle operation.

from the same crow-bar current issue as the level-shifter.

The solution to this problem is shown in Fig. 3.6 and utilizes a modified driver chain with both 5 V and 32 V from the on-chip HV supply to generate non-overlapping 5 V and 32 V gate voltages, thus eliminating crow-bar current in the output driver. The input pulse is first shifted-up to 5 V, providing the drive signal for the output HV-NMOS and then level-shifted to 32 V to drive the output HV-PMOS. In this configuration, the 5 V level-shifter is designed with 5 V transistors for higher drive strength and smaller parasitics compared to the 32 V HV transistors. Meanwhile, the 5 V boosted signal is also used as the input of the 32 V shifter, such that M_{i+} in the level-shifter is driven by 5 V, improving both its efficiency and the circuit bandwidth compared to the design driven from the 1.8 V input.

Finally, in order to further increase the drive strengths, large HV-NMOS and HV-PMOS are used as the output buffer. HV-NMOS and HV-PMOS are driven by 5 V and 32 V sources, respectively, considering the tradeoff between the output driving ability, power consumption, and circuit area.

In order to avoid crow-bar current at the output, the driving signals of the 2 HV-MOS are designed to be non-overlapping. First, a cross-coupled level-shifter with a total of 3 shifter

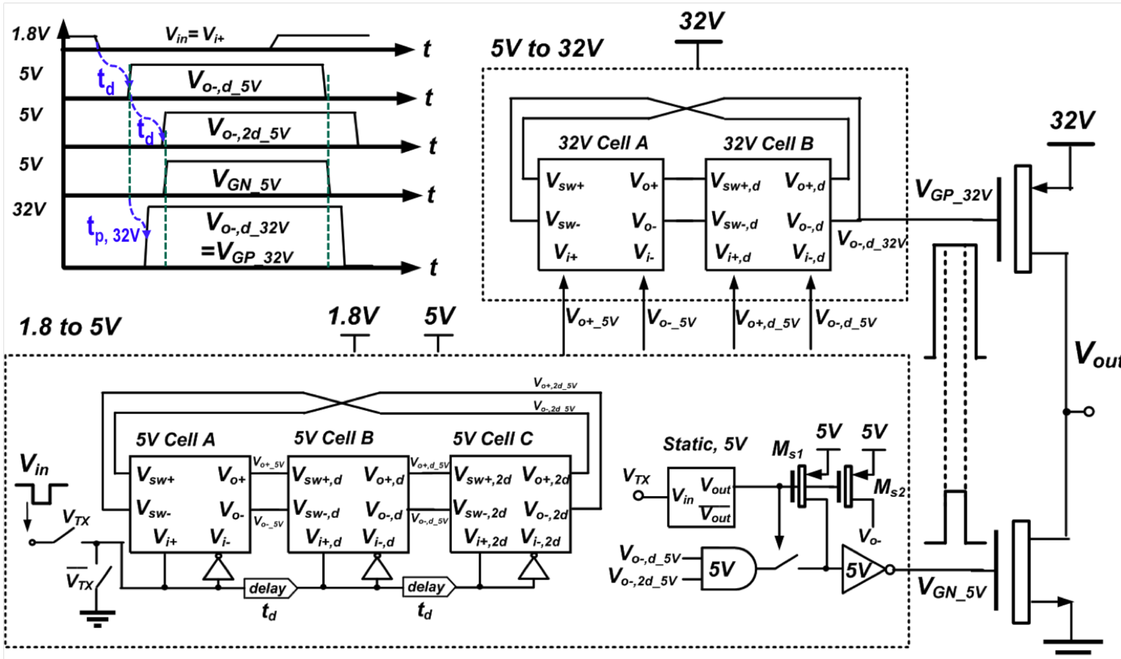

Figure 3.6: Block diagram and signal waveforms of the HV driver chain.

cells takes the 1.8 V input and generates 3 sets of differential 5 V outputs, separated by t_d = 5 ns as shown in the timing diagram in Fig. 3.6. Second, differential outputs of 5 V Cell A and 5 V Cell B, V_{o_5V} and V_{o,d_5V}, respectively, are used to generate 32 V outputs using a cross-coupled 32 V shifter cells. V_{GP_32V} used drive the HV-PMOS is the negative output of 32 V Cell B, while V_{GN_5V} to drive the HV-NMOS is generated from the negative outputs of 5 V Cell B and 5 V Cell C, V_{o-,d_5V} and $V_{o-,2d\_5V}$, respectively.

With this configuration, the falling edge of V_{GN_5V} follows the falling edge of V_{o-,d_5V}, which always happens before the falling edge of V_{GP_32V} due to the propagation delay $t_{p,32V}$ = 3 ns of the 32 V shifter. Similarly, the rising edge of V_{GN_5V} follows $V_{o-,2d\_5V}$, which is designed to rise later than the rising edge of V_{GP_32V}. As shown in Fig. 3.6, as long as t_d is larger than $t_{p,32V}$, the resulting non-overlapping gate driving voltages, V_{GN_5V} and V_{GP_32V}, can eliminate crow-bar current at the output MOS driver. In this design, the MOS driver is designed to provide 53 mA on average, suitable for driving a 25 pF load at up to 40 MHz frequency. The parasitic capacitance at the output node with the driver size is 0.9 pF.

When the system is switched to the receive mode, V_{TX} switches from high to low, in order to ground V_{in}. This results in V_{o-_32V} to rise to 32 V, turning off the HV-PMOS. At the NMOS side, M_{s1} and M_{s2} are activated to pull the output of the NAND gate to 5 V and recharge V_{o-_5V} and hence V_{GN_5V} to ground, effectively turning off the HV-NMOS. The high-voltage driver is then disabled and becomes a parasitic capacitive load that attenuates the received signal.

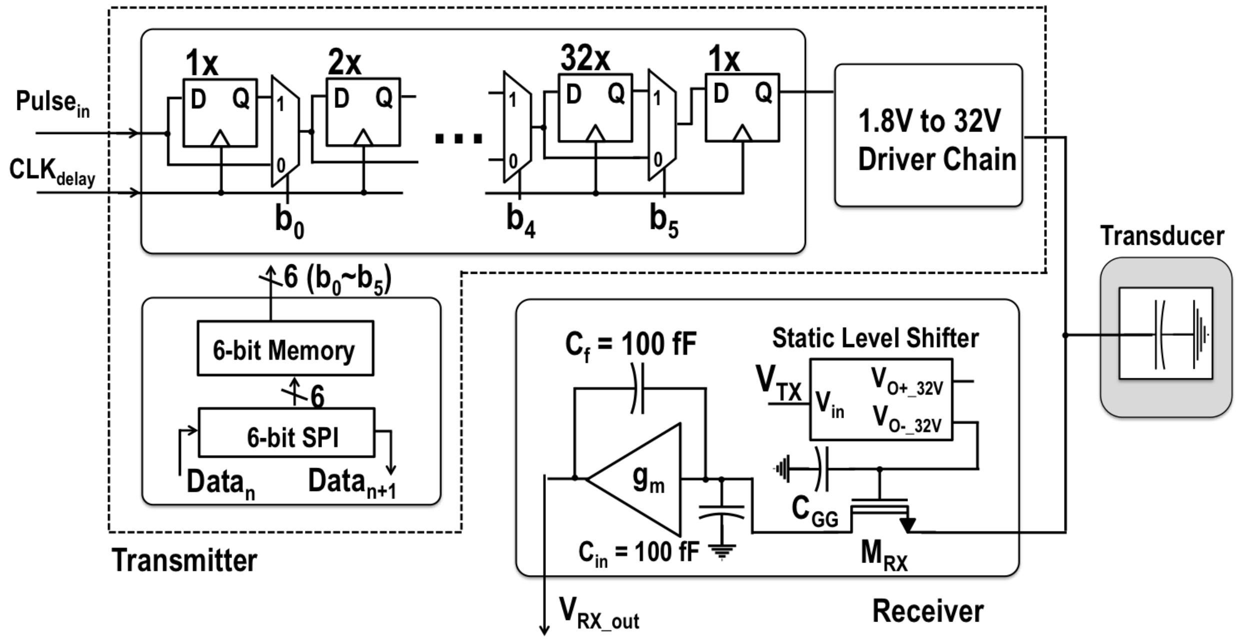

Figure 3.7: Block diagram of one channel, showing the receiver front-end and the delay-chain.

Receiver Preamplifier

As the system switches to the receive mode, the receiver protection switch closes and the output node connects to the low-voltage receiver and waits for the incoming signal generated from the incident pressure to the transducer as shown in Fig. 3.7. The switch M_{RX}, however, is also a high-voltage device that can withstand the HV drive voltage. Hence, static level-shifters are used to shift-up the gate driving signal. Given that the driving voltage of the gate is 32 V, the switch can be sized down to reduce the input parasitics of the amplifier, as well as the gate capacitance C_{gg} to save power.

Delay Control Block

A 6-bit delay control block is implemented in each channel for the beamforming operation. As shown in Fig. 3.7, the delay control block consists of a 6-bit SPI and a 63 DFFs delay chain with the shared clock, CLK_{delay} with a period of T = 5 ns in this design. The SPI output controls each MUX to select the delay written in the SPI to determine the number of DFFs the input signal passes through. The delay amount t_d of each channel is then given by $t_d = M \times T$, where $M = b5...b0$ is the digital number written into the SPI. A clock-tree layout is implemented to minimize skew or mismatch among DFFs. The last DFF in the delay chain synchronizes each channel input and aligns them to the rising-edge of CLK_{delay}.

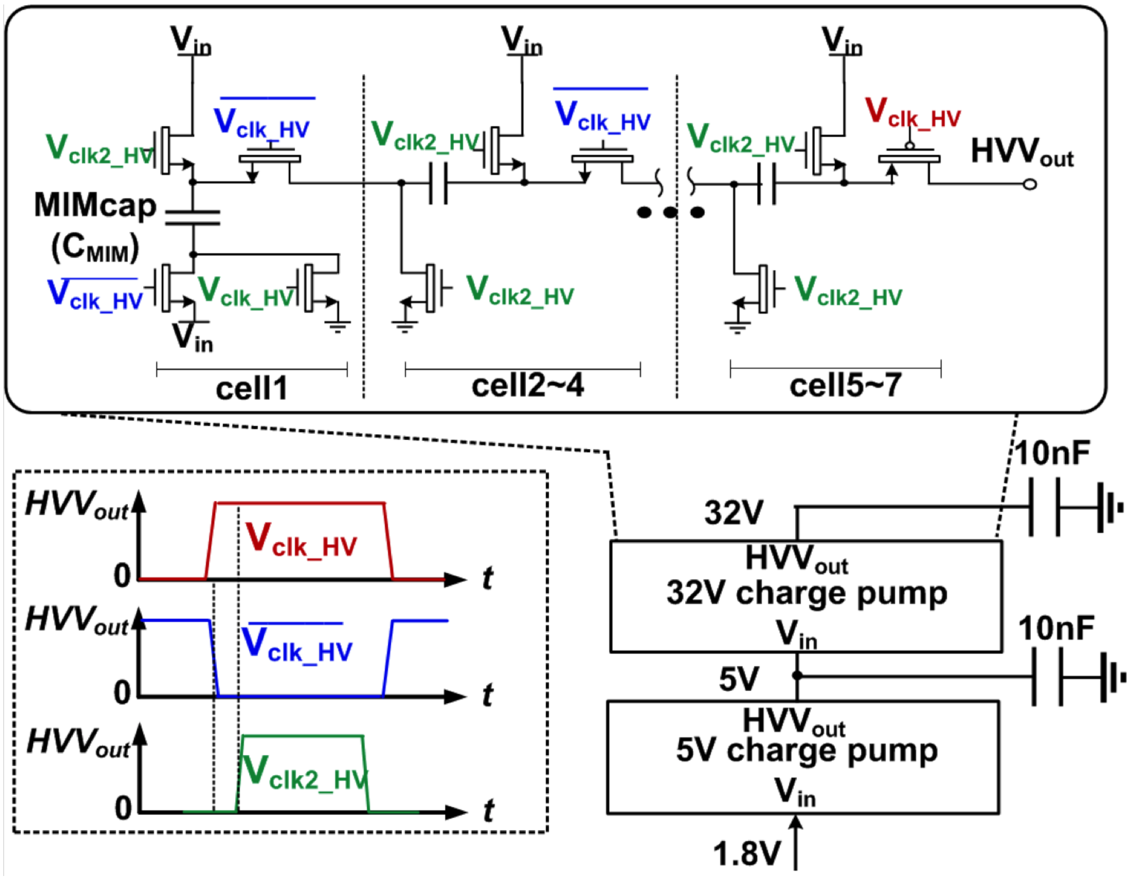

Figure 3.8: Charge pump block diagram and its required clock waveforms.

Charge Pump Design

In the previous sections, we discussed the level-shifter design that shifts the 1.8 V pulses up to 32 V, assuming that the 5 V and 32 V DC supplies are provided. In this section, we discuss the DC-DC converter design that provides these high-voltage DC power lines from a single 1.8 V power supply.

The total step-up ratio from 1.8 V to 32 V is greater than 18, which makes it difficult to achieve high conversion efficiency. Therefore, we implement a two-stage step-up design with the intermediate 5 V output voltage, resulting in the step-up ratio of 3 and 7, respectively. This design has an added benefit in that the intermediate 5 V output voltage can also be used in the driver chain to improve both the driving speed and the efficiency, as previously mentioned.

Fig. 3.8 shows the overall charge pump diagram. This design employs a series-parallel architecture [24] instead of a voltage doubler, in order to stay within the breakdown voltage limit of compact, high density, and small bottom plate capacitance of 5 V MIM capacitors.

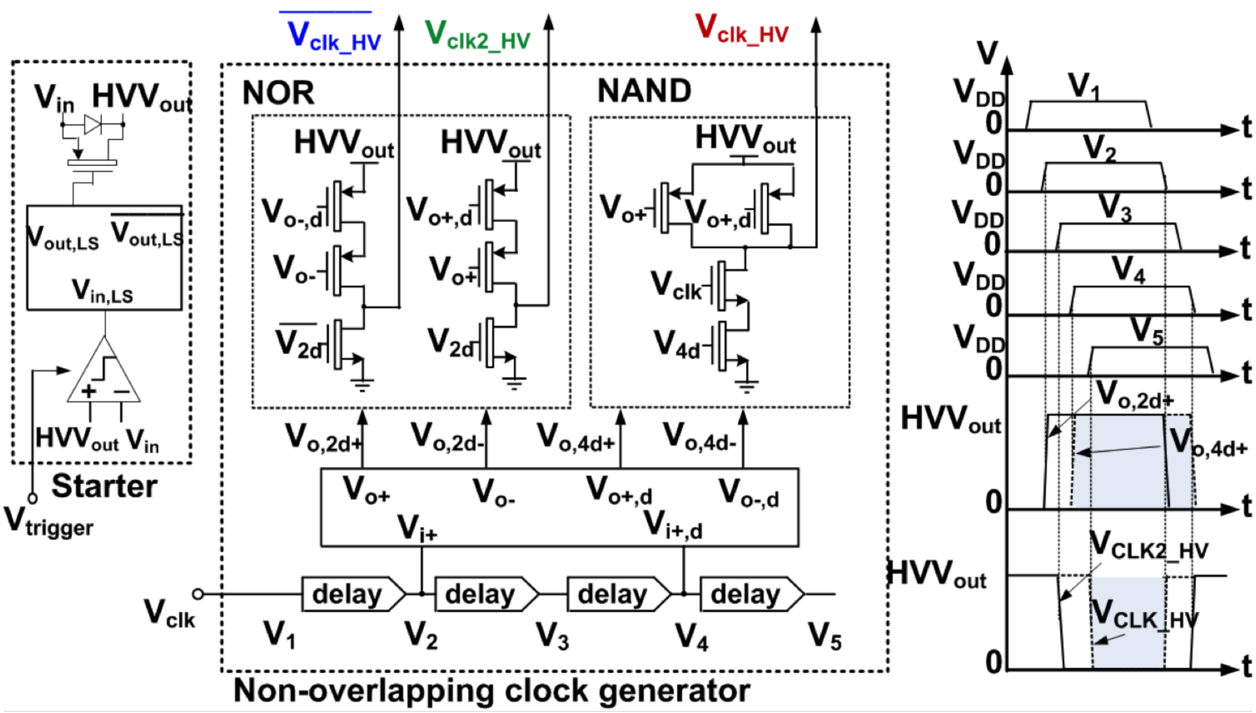

Figure 3.9: Charge pump clock generator circuit and its waveforms.

For the 5 V and 32 V charge pumps, two and seven cells are used, respectively. Unlike the previous work in [24], which employs a traditional AC-coupled switch driving scheme, this implementation relies on the level-shifter described above to avoid the need for high-voltage capacitors and provide a rail-to-rail driving signal, resulting in smaller switches and improved efficiency due to their smaller parasitic capacitances.

To reduce the switching loss, the charge-pump requires not only one, but multiple non-overlapping control signals for the 2 phases of the charge pump. However, traditional methods of generating non-overlapping clocks using delay cells or inverters are not acceptable in the high-voltage domain due to the crow-bar current issue. One solution is to generate non-overlapping signals in low voltage domain and shifting them up to the high voltage domain using separate level-shifters. In our case, we can take advantage of the inherent multiple phase outputs of the proposed dynamic level-shifters to generate non-overlapping control signals, thus saving area.

Fig. 3.9 shows the block diagram of the HV clock generator circuit and its output waveforms. A series of delay cells with delay $t_d \sim 1\mu$s are used to generate low-voltage inputs, $V_1 - V_5$ with 5 difference phases. V_2 and V_4 are used for dynamic level-shifter inputs to generate four HV outputs $V_{o,2d\pm}$ and $V_{o,4d\pm}$ with negligible propagation delays compared to t_d. The first high-voltage clock signal is generated by passing through high-voltage NAND structure with $V_{o,2d+}$ and $V_{o,4d+}$ as the pull-up gate controls, while the low-voltage signals V_1

and V_5 control pull-down switches. With this configuration, pull-down switches are always turned off before pull-up switches closes and turned on after pull-up switches are both opened in order to avoid crow-bar current. The consequent output clock signal, V_{clk_HV+}, thus follows the rising edge of V_4 for its high-to-low transition and the falling edge of $V_{o,2d+}$ for its low-to-high transition, as indicated by the timing diagram in Fig. 3.9. Similar topology can be applied to a NOR-like structure to generate the rest of the 2 signals: V_{clk_HV-} with its transition following V_3- rising and $V_{o,4d-}$ falling, and V_{clk2_HV} with V_3+ rising and $V_{o,4d+}$ falling. The resulting HV non-overlapping waveforms are shown in the Figure; the transition edges of V_{clk_HV+} and V_{clk2_HV} are separated by t_d, which is suitable for the charge pump operation.

Finally, the HV non-overlapping circuit is not used in the main driver chain since the high-voltage NAND and NOR, though efficient, have fairly low speed due to the 1.8 V input voltage.

3.4 Measurement Results

Test Setup

The ASIC was fabricated in 0.18 μm 32 V CMOS with 5 V and 32 V HV transistors and 5 V MIM capacitors. For this prototype, the entire ultrasonic system consisted of a custom ASIC and a bulk piezoelectric transducer array, and to reduce the system complexity, data conditioning and processing were done with an Opal Kelly FPGA-USB module, off-chip ADCs, and buffer amplifier with 0.1 MHz to 5 MHz bandpass filters. A chip micrograph and the overall system, shown in Fig. 3.10, contained 7 integrated front-ends which included TX beamformer, HV driver, HV DC-DC converter, and RX front-end. The active chip area was 1 mm×2 mm and the entire platform measured 5 cm×7 cm, dominated by the FPGA board.

System Performance

The system operated from a single 1.8 V supply and generated driver output pulses up to 32 V. The static power dissipation in the dynamic level-shifter was negligible. The measured output waveform of the driver chain with the beamformer delay set to zero is shown in Fig. 3.11. With a 8 pF probe output load, the 50-50 latency was 28 ns from the low-voltage input to the high-voltage driver output and was limited by the propagation delay of the driver chain and t_d. The measured driving efficiency, defined as $C_L \cdot (HVV_{DD})^2/P_{in,32V}$, was 89%, where $C_L = 8$ pF, $HVV_{DD} = 32$ V, and $P_{in,32V}$ was the power drawn from the 32 V source. The measurements were made with on-chip supplies.

The 5 V and 32 V charge pumps used 250 pF and 100 pF series on-chip MIM capacitors and operated at 2 MHz and 60 kHz, to deliver 91 μA and 5 μA, respectively. This was sufficient to perform measurement every 21.3 ms with 6 cycles of 3.2 MHz, rail-to-rail 32

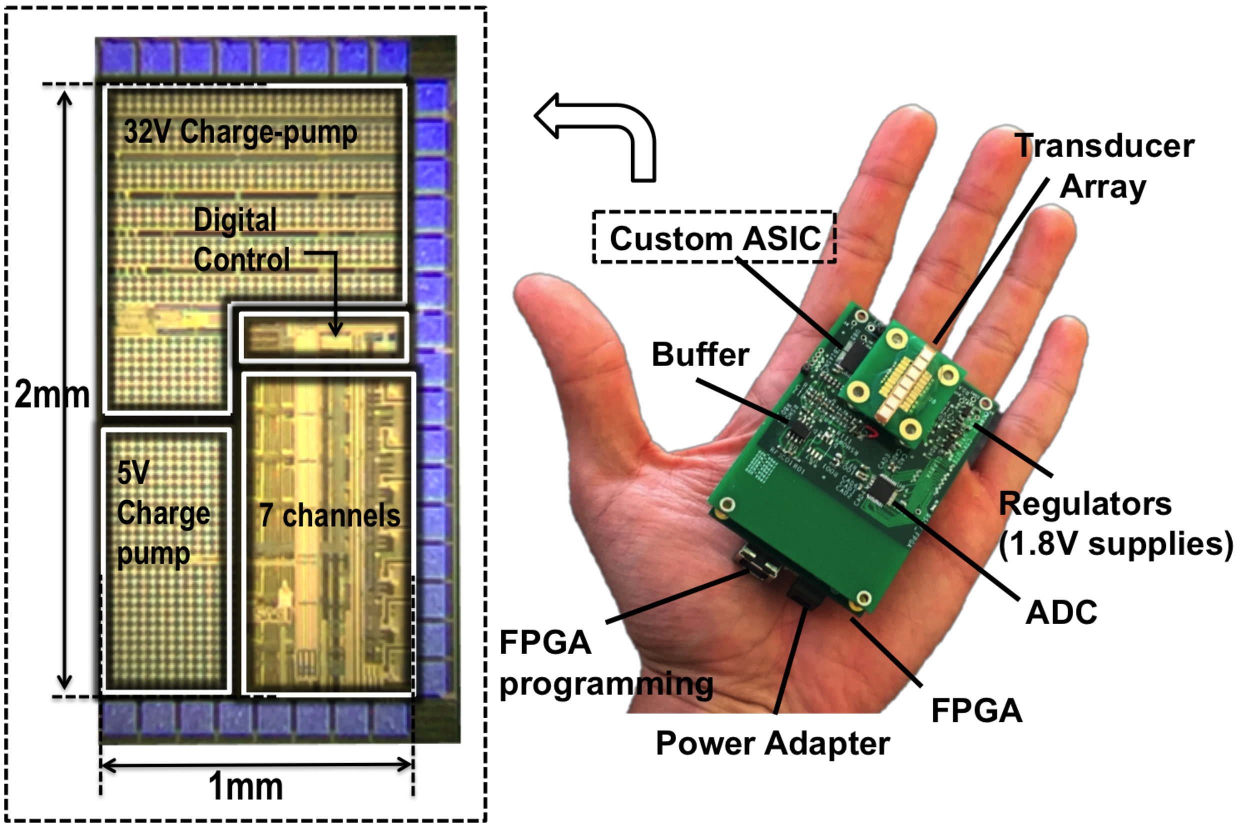

Figure 3.10: System and die photo of the custom ASIC.

V pulses driving each transducer. Fig. 3.12 shows the start-up transient waveforms of the cascaded 5 V and 32 V charge pumps and their performances with 10 nF bypass capacitors. The output reached 90% of the final value after 37.6 ms. With a 60 kHz clock, the charge pumps achieved over 30% efficiency and delivered up to 160 μW.

The level-shifter was capable of operating at up to 40 MHz. The latency between the input pulse to the fixed output load of 8 pF was 28 ns. The latency increased to 52 ns with our transducer array, which had a measured load of $C_L = 80\,pF$ per channel. The input-referred noise level of the system was 35 μV within the signal band of 0.1 MHz to 5 MHz.

3.5 Conclusion

In this chapter, we present an ultrasonic ASIC that integrates high-voltage supplies and efficient high-voltage drivers. The performance of the level-shifter, the HV driver, and the charge-pump has been test and verified. In the next chapter, a imager system is built with

Efficiency	Max. Operating Frequency	Latency
89%	40MHz (8pF load)	28ns

$$*\text{Efficiency} = C_L(HVV_{DD})^2 / P_{in(32V)}$$

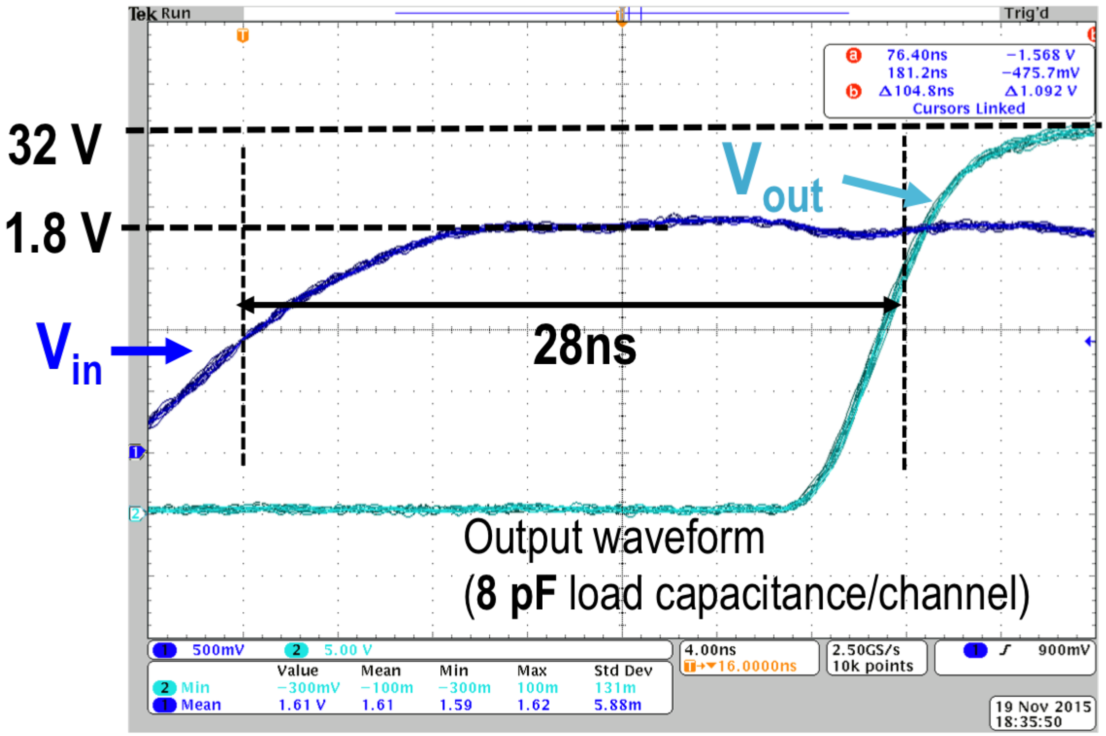

Figure 3.11: Scope waveforms of the driver chain output.

the proposed ASIC to demonstrate the capability of the system.

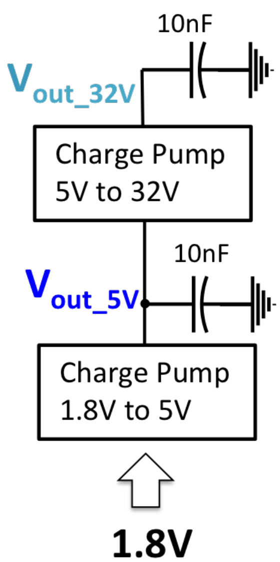

	5V charge pump	32V charge pump
CLK frequency	2-MHz	60-kHz
# of stages	2	7
Efficiency	93%	35%
Output current	91-µA	5-µA

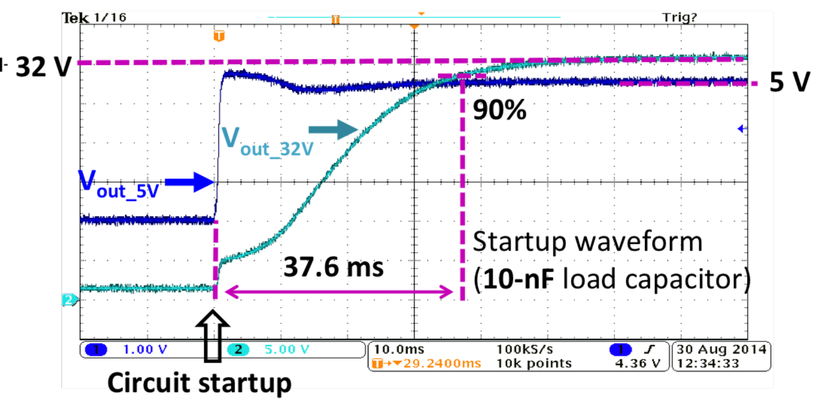

Figure 3.12: Charge pump start-up waveforms and the performance summary.

Chapter 4

Miniaturized Ultrasonic Imager for Personal Fitness Tracking

4.1 Motivation

Recently we have witnessed an increasing interest in personal fitness, supported by a proliferation of devices that track personal activity such as number of steps taken in a day or sleep patterns. The expectation is that this information will help individuals adapt their lifestyle and well being. One challenge is that the assessment of changes is highly subjective. Lack of accurate and objective feedback can reduce the motivation and result in spotty adherence to or abandonment of lifestyle changes.

The body mass index (BMI) provides objective feedback and can be inferred from a simple impedance measurement that is integrated in many consumer grade scales. Unfortunately, the measurement is susceptible to a long list of co-factors including humidity and daily variations of metabolic activity that reduce the accuracy. Moreover, the BMI gives only global information for the entire body and fails to provide insight into specific areas such as the abdomen that are of particular interest.

Medical ultrasound can be used to accurately assess body composition [5]. Figure 4.1 shows an ultrasound image of the abdominal region. In this image, the skin, fat, and muscle layers can be clearly separated. Regularly assessing the thickness of the various layers gives objective and accurate feedback about changes as they are occurring. Unfortunately, the cost, size, power dissipation and complexity of medical ultrasound equipment renders this solution inadequate for consumer use.

However, current ultrasonic systems are expensive, bulky, highly complex, and power-hungry. In this work, we present an energy-efficient high-voltage dynamic level-shifter architecture and charge-pumps that enable integration of high-voltage generation on-chip. With the ASIC [20] we built that is a complete, fully-integrated 7-channel ultrasonic imager, we could design a portable ultrasound imager that enables a compact and low power solution.

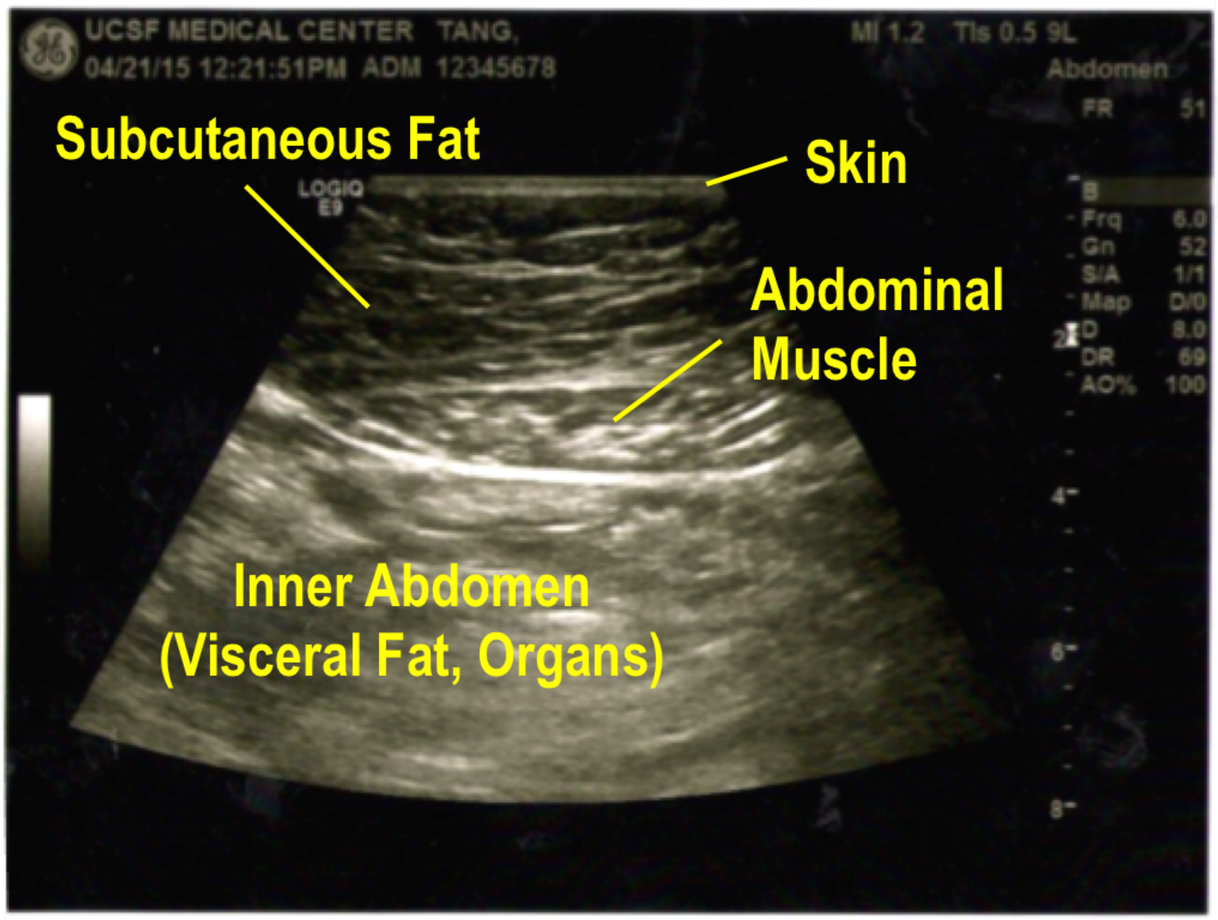

Figure 4.1: Ultrasound image of the abdominal region recorded with a commercial medical ultrasound system (GE Logiq E9). The skin, fat and muscle boundaries are clearly visible.

4.2 System Architecture

Figure 4.2 shows the ultrasonic imager comprising the transducer array and the ASIC assembled on a carrier PCB connected to a daughter board, buffer amplifiers, the ADCs and the digital control. The entire assembly is packaged in a ABS enclosure. Only the transducer is exposed, with PDMS caulking protecting the electronics and interconnects from water and coupling gels used during measurements.

Seven element transducer array was assembled on a daughter PCB using pre-metalized Lead Zirconate Titanate (PZT) sheets from APC International Ltd. Each element measured 3 mm $\times$ 3 mm and had resonant frequencies and bandwidth of $\sim$3.2 MHz and $\sim$0.5 MHz, respectively. The element pitch was $\frac{15}{2}\lambda \sim 3.5$ mm. Each element was modeled using a

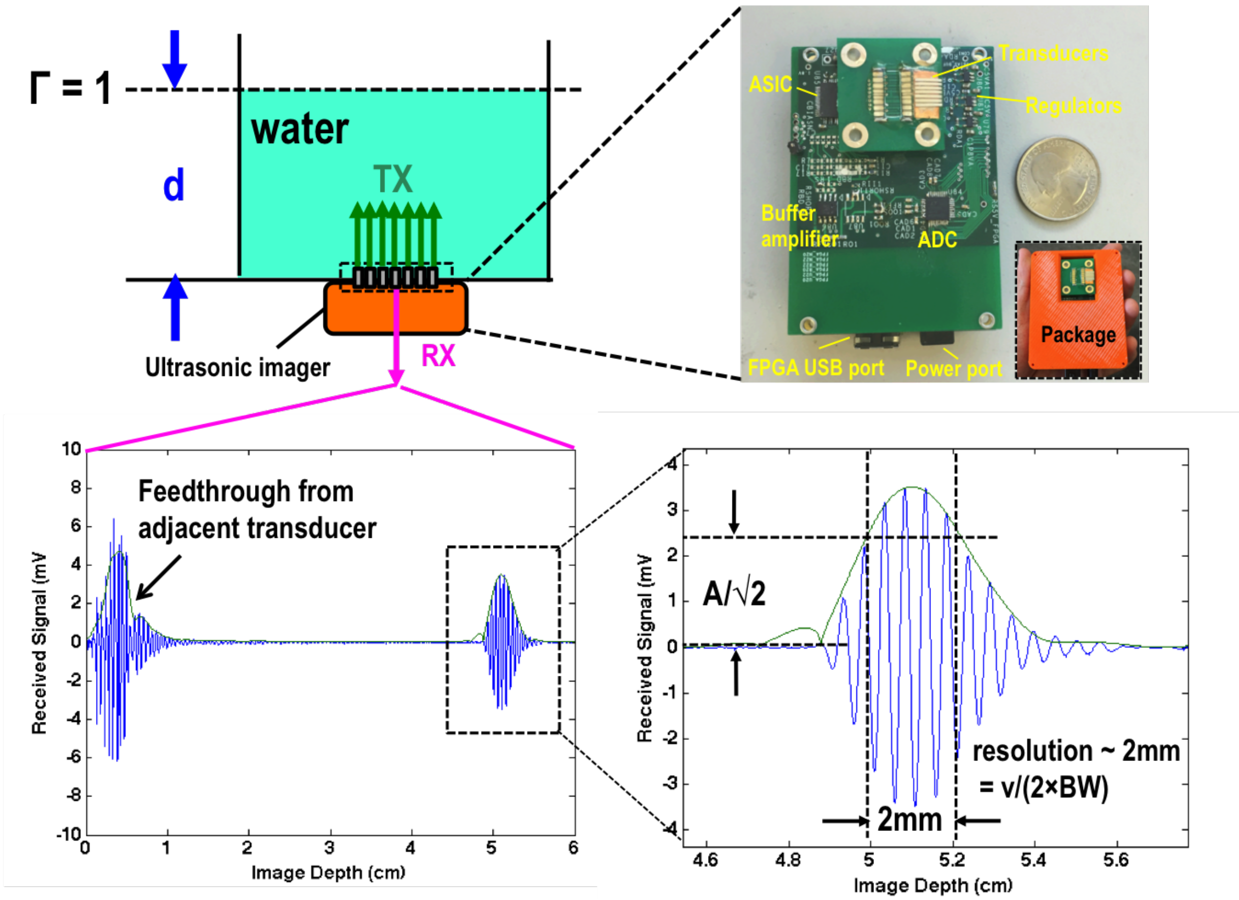

Figure 4.2: Test setup and the received signal of the system.

simple series equivalent circuit model near resonance [25]]. The array was designed and simulated with the MATLAB package USIM [26]. The detailed design procedures for an ultrasonic array can be found in [27], [28].

Each PZT element was electrically connected to the corresponding channel in the ASIC by a conductive copper foil and epoxy for the bottom terminal and a wirebond for the top terminal. Finally, the array was encapsulated in PDMS to protect the wirebond and provide insulation. The entire array measured 24 mm $\times$ 3 mm.

In this paper, each element was chosen to be relatively large in order to maximize the SNR of the received echoes. Given the large aperture, each element was quite directional and the Rayleigh distance of the entire array was close to 30 cm. Therefore, the array was driven with zero delays (i.e., no beamforming) in this paper. Detailed treatment and the measurement results of the beamforming capabilities with a smaller transducer array could be found in [29].

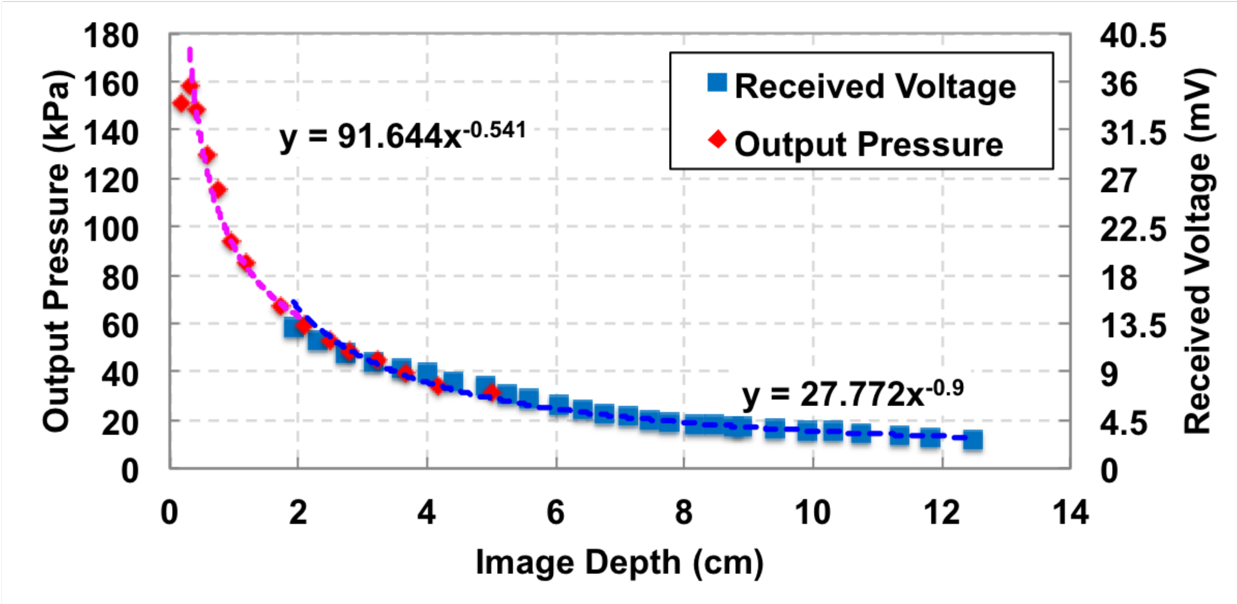

Figure 4.3: The relationship between the received signal and the image depth was used to time-gain compensate 1/R loss from beam spreading.

4.3 Measurement Results

SNR Measurement with Liquid-Air Interface

Figure 4.2 shows a measured echo from a water-air interface that confirms the depth resolution of 2 mm set by the transducer bandwidth. Due to a large difference in their acoustic impedances, the liquid-air interface reflected close to 100% of the incident ultrasound waves.

In order to further determine the SNR at various image depths, the transducer array was encased in a cylindrical tube, with a diameter and a height of 6 cm and 8 cm, respectively, and the amount of water in the tube was varied to create the interface at different transmission distances. Since the liquid-air interface was close to a perfect plane reflector, the image depth was 2 times the water depth.

Fig. 4.3 shows the maximum amplitude of the received pulses as a function of the image depth. For an image depth below 2 cm, a capsule hydrophone was used to measure the output pressure. Note that the wave propagation distance is two times of the image depth. Hence in the graph, the distance of the hydrophone measurement is divided by 2 to indicate that the pressure at distance x corresponds to an image depth at $x = d/2$.

The output pressure at the surface of the transducer was ~160 kPa. We observed an initial inverse quadratic dependence followed by an inverse relationship between the amplitude and the transmission distance at ~3 cm away, representing the transition between the near and far-field of an array. This data was used to time-gain compensate (TGC) 1/R loss due

The received voltage at 12 cm was >3 mV, which was significantly larger than the input noise of the system at 35 μV. Therefore, the achieved SNR of the system was sufficient beyond 10 cm for the liquid-air interface. For fat/muscle thickness measurement, the limit on the range was imposed by the small reflection coefficient of fat-muscle boundary at ∼10% [3].

Phantom Measurement

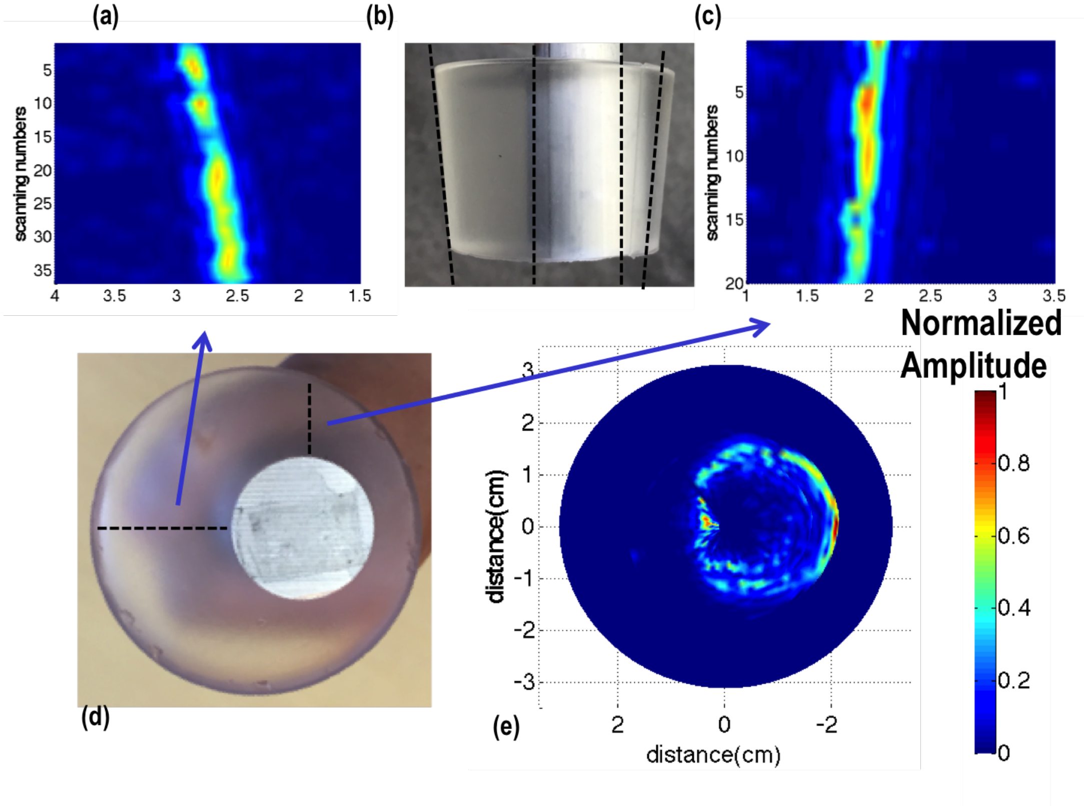

Figure 4.4: A steel rod encased in PDMS was used as the phantom. The side and top view of the phantom, (b) and (d), respectively, and their corresponding 2-D sonographs are shown in (a), (c), and (e).

to beam spreading.

In order to demonstrate 2-D sonograph capabilities, a steel rod encased in a PDMS mold was prepared as the phantom as shown in Fig. 4.4. The transducer array was put in contact with the phantom and manually moved along and around the phantom. The transducer was driven with 6 cycles of 32 V pulses at its resonance frequency of 3.2 MHz to emit ∼160 kPa ultrasonic pulses into the phantom. The resulting TGC 2-D side and radial scan of the phantom are shown in Fig. 4.4a and Fig. 4.4c and Fig. 4.4e, respectively, with clearly

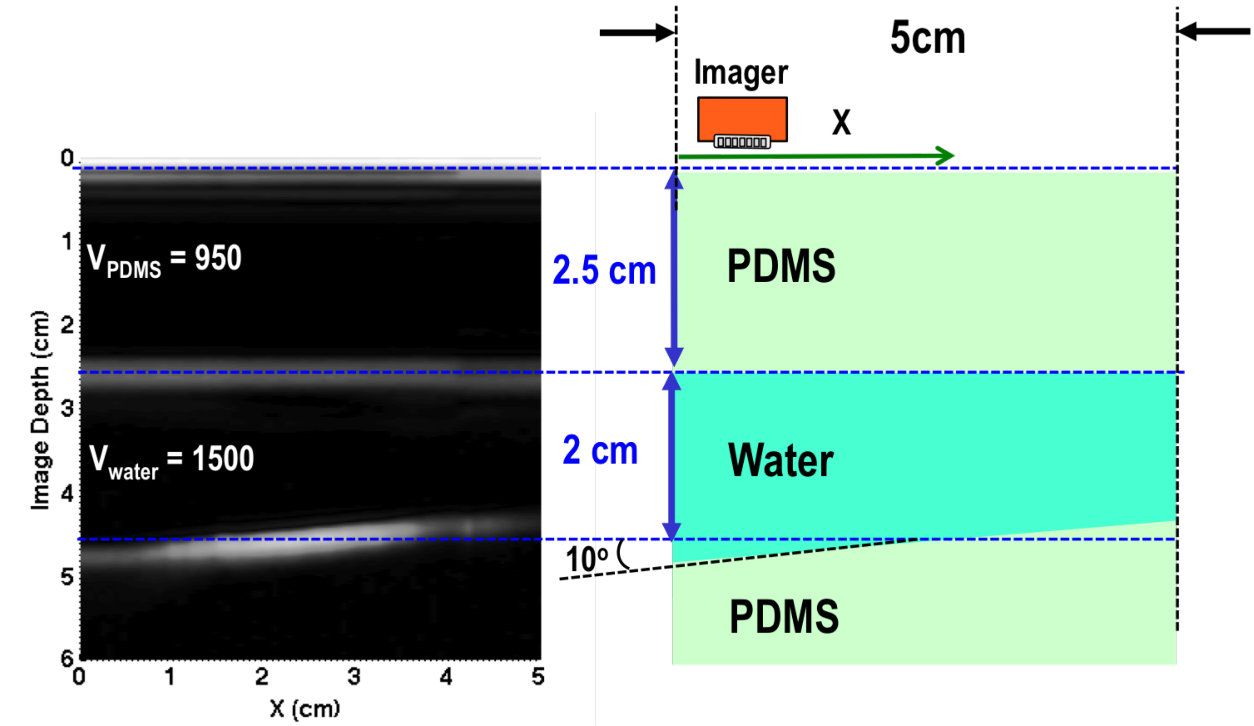

Figure 4.5: Test setup and time-gain compensated 2-D sonograph of a 3 layers phantom comprising 2 PDMS layers and water.

identified edges.

Each side and radial scan consisted of approximately 30 and 60 sites, respectively, with 5 measurements per site, that were stitched together. The total scan time was approximately 4 and 8 seconds, respectively.

Another measurement is evaluated with a phantom shown in Figure 4.5. The phantom consist of 2 PDMS layers with water in-between, mimicking the fat-muscle-fat structure in the human abdomen. In this experiment, the imager is mechanically stepped through 80 positions along the horizontal axis. The received signal strength is scaled with the inverse of the depth to correct for the $1/d$ spreading loss.

In-Vivo Measurement

Finally, the system was evaluated *in-vivo* on human. The transducer array was placed in contact with a person and the ultrasonic gel was used to ensure good coupling between the device and the skin. In order to avoid the huge reflection at the transducer-skin boundary potentially saturating the system, the RX preamplifier was kept in reset mode while waiting

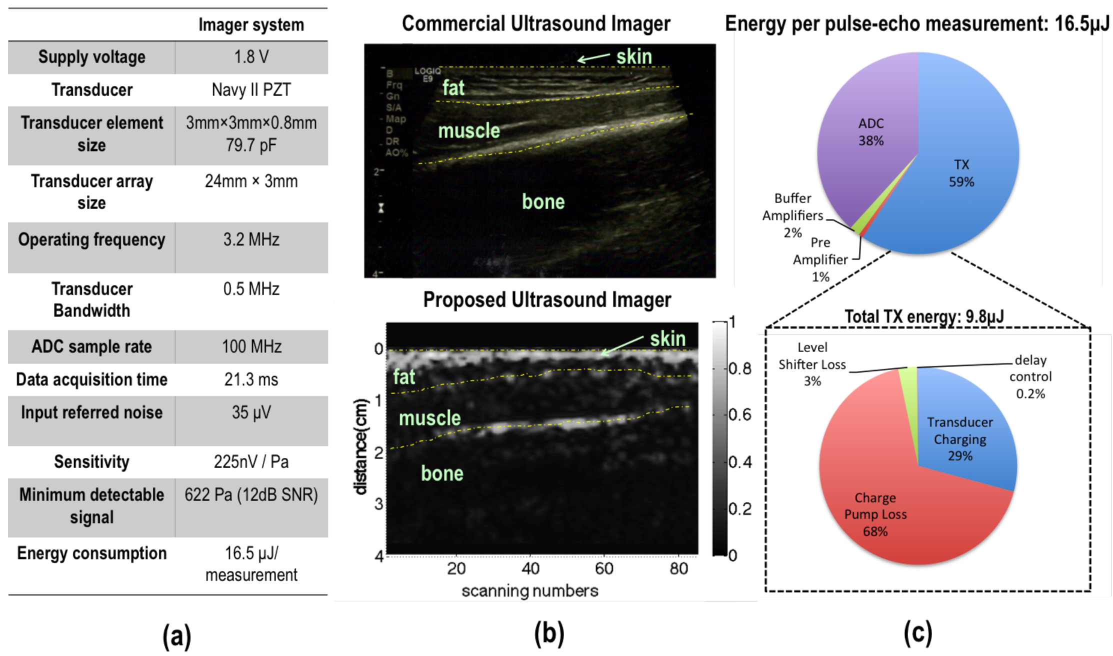

Figure 4.6: (a) Imager performance summary, (b) the power breakdown chart, and (c) Comparison of measurement from a commercial ultrasound imager and the proposed imager.

for the skin echo. Upon detecting the skin echo, the reset switch opened and the subsequent echoes were amplified with a gain of 28 dB.

A 2-D scan of a human arm was first obtained using a commercial medical ultrasound machine (LOGIQ E9) as shown in Fig. 4.6. We obtained a similar TGC 2-D sonagraph using our imager, shown in Fig. 4.6, by placing the transducer array on the same spot and manually sliding the imager. The fat, muscle, and bone layers were clearly visible in both scans, resulting in ~ 9 mm and 11 mm of fat and muscle thicknesses, respectively. The slight mismatch between two figures could have resulted from non-uniform scanning speed using our imager or a change in the body composition between the two scans. Despite the image quality is inferior to the commercial ultrasonic imager, the proposed imager system consumes significantly less amount of power with size much favorable for consumer electronics.

Each pulse-echo measurement took 67 μs to image as deep as 5 cm and consumed 10.5μJ, 0.14 μJ and 5.8 μJ of energy for TX, RX buffer, and ADC, respectively. Limited by the charge-pump output power, the system performed measurement every 21.3 ms. The in-vivo 2D scan in Fig. 4.6 consisted of 100 pulse-echo measurements and hence the entire image took $\sim$2.2 s to obtain. The overall system performance and the power breakdown are summarized in Fig. 4.6c.

Another measurement is performed and shown in figure 4.7 as an ultrasonic image of a human abdomen. A coupling gel (Acquasonic Inc.) is used to ensure good signal transmission. The transducer is manually slid over a 5 cm section of the abdomen. The boundaries

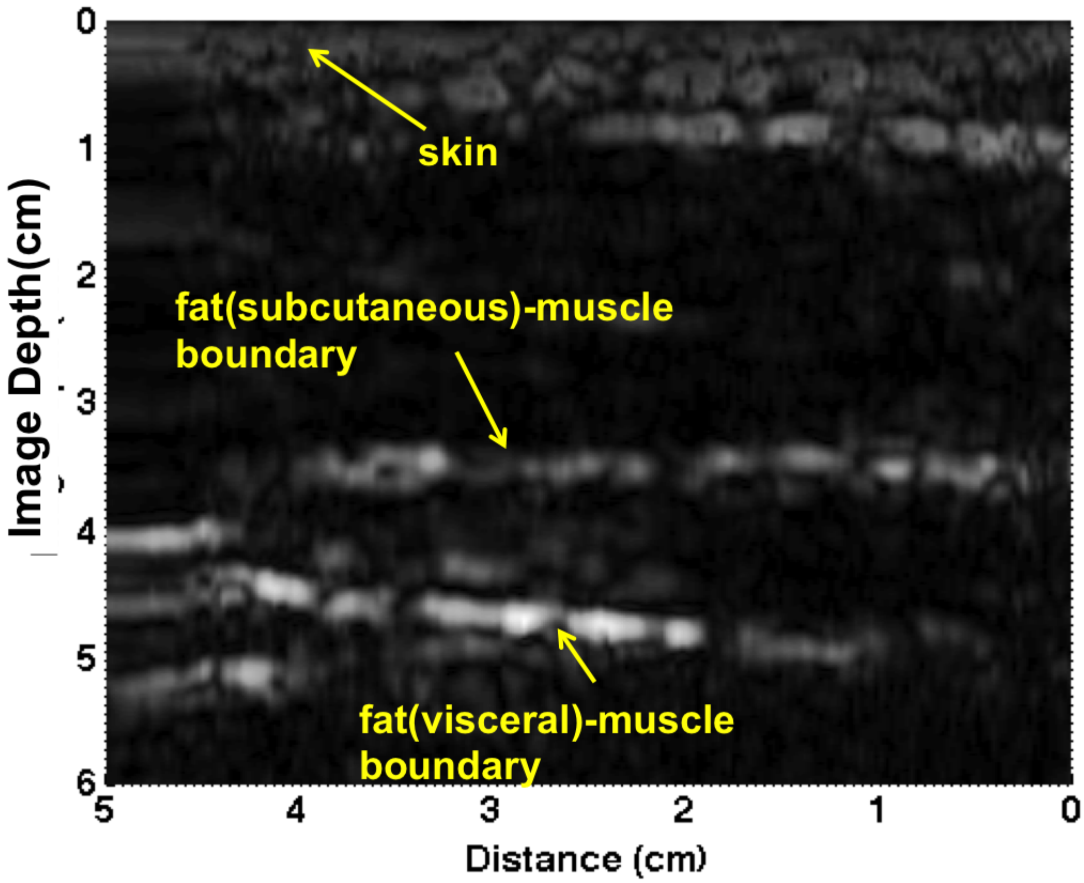

Figure 4.7: In-vivo 2-D sonograph of human abdomen imaged by the proposed miniature ultrasound imager

between the muscle and subcutaneous and visceral fat layers are clearly visible and indicate that the test subject has 10 . . . 15 mm muscle under approximately 35 mm skin and fat.

Table I summarizes the transmitter performance of this work compared to state of the art designs from industrial and academic researchers [11], [17] – [19]. In [17], Chen et al. implemented a tri-level driver design that reduced the dynamic power consumption from CV_{DD}^2 to $0.5CV_{DD}^2$, at the cost of reducing both operating speed and the driving strength. However, the techniques proposed in [17], if implemented along with the proposed dynamic level-shifter and charge pump, can result in further improvements in the power efficiency, as well as circuit bandwidth. Furthermore, to the best of the authors' knowledge, the proposed work is the only one that can operate with a single 1.8 V supply. An energy-efficient high-voltage dynamic level-shifter architecture and charge pumps that integrated

Table I: Comparison of ultrasound imager TX performance

	This Work	ISSCC'13 [10]	JSSC'13 [16]	TI [17]	TCASII'14 [18]
Supply voltage	1.8 V	1.8, 60 V	3.3, 30 V	1.8, 3.3, ±5, ±10, ±40, ±50 V	1.8, 15 V
Output Pulse	0~32 V	0~60 V	0~15~30 V	-48.5~0~48.5 V	0~15 V
Channel Numbers	7	32 × 32 * flip-chip bonding	4	8	1
Nominal Load Capacitance	80 pF	2.5 pF	40 pF	330 pF	12 pF
Efficiency ($HVV_{DD} \rightarrow C_L$)	89%	--	>100%* *Tri-level design	--	--
Static Power	0	--	0	70 mW	0
Delay control resolution	5 ns	10 ns	10 ns	N/A	N/A
Nominal frequency	3.2MHz	5 MHz	3.3MHz	5 MHz	2.6MHz
Maximum Frequency	40 MHz *with 8pF load	20 MHz	5.2MHz	15 MHz	--
Minimum Latency	28 ns *with 8pF load	N/A	N/A	32 ns	30.8 ns
Chip area	2.0 mm^2	84.6 mm^2	0.6 mm^2	--	0.15 mm^2
Technology	TSMC 0.18um HV	0.25um HV	TSMC 0.18um HV	--	0.18um HV

all high-voltage generation on-chip achieved state-of-the-art operation frequency and latency while maintaining comparable chip area to other works.

4.4 Conclusion

In this chapter, we present an ultrasonic imager that integrates high-voltage supplies and efficient high-voltage drivers. A series of experiments are performed, both with phantoms and *in-vivo* on humans, to verify the system functionality. The imager has a measured sensitivity of 225 nV/Pa, minimum detectable signal of 622 Pa assuming 12dB SNR (4σ larger than noise level), data acquisition time of 21.3 ms, and can image human tissue as deep as 5 cm in under 70 μs while consuming less than 16.5 μJ per measurement. The system performance is comparable to that of a traditional ultrasonic imaging system, but at a fraction of the power consumption and size. The overall size and efficiency of the system are significantly improved due to a custom ASIC that fully integrates high-voltage generation and efficient driving circuits and schemes to reduce static power consumption.

Chapter 5

3D Ultrasonic Fingerprint Sensor-on-a-Chip

5.1 Introduction

Recurrent security breaches in the public and private sectors set pressing need for improved standards compared to text-based password systems that can be easily compromised. More robust and personalized security measures become increasingly more important as the number of devices we interact with increases. Recently, bio-metrics-based systems, such as those using fingerprints, have been incorporate into a wide variety of devices, including smart phones, watches, or door-knobs to provide naturally secure access without the inconvenience to the users.

Present fingerprint recognizers fail to meet the reliability, size, and cost constraints of consumer applications. Optical sensors are difficult to miniaturize and easily spoofed. Capacitive approaches meet the size and cost targets but suffer from susceptibility to humidity and contamination. Ultrasound-based fingerprint sensors address these shortcomings. For example, the image quality of ultrasonic fingerprint sensors is weakly affected to contamination and humidity. Fig. 5.1 shows the comparison of a 4.73 mm×3.25 mm fingerprint image of a wet finger captured by a commercially available capacitive fingerprint sensor [30] with the image produced by the ultrasonic fingerprint sensor presented in this chapter. Even after drying with tissue paper, the large difference in the permittivity of a moist finger affects the image quality of capacitive fingerprint sensor.

Another advantage of ultrasonic fingerprint sensors is their abilties to capture not only the fingergprint visible at the surface but to also gather information inside the tissue usually referred to as epidermal and dermal fingerprints [31], respectively. Fig. 5.2a shows the epidermal and dermal fingerprint images produced by the sensor. For reference, fig. 5.2b shows an ultrasound sonograph of a human finger with 50 MHz ultrasonic pulses reported in [32]. Imaging the "inner" dermal surface of the finger in addition to the surface has two

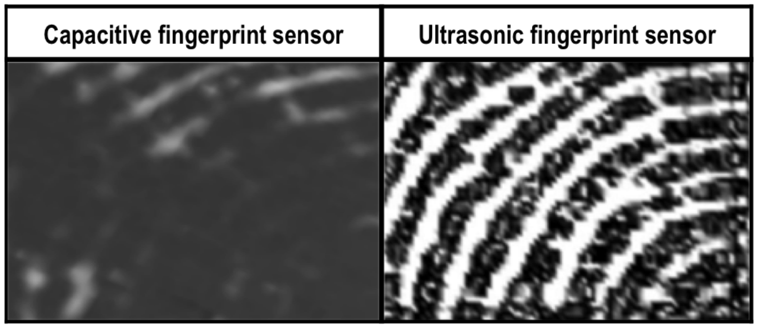

Figure 5.1: Fingerprint captured with capacitive [30] and ultrasonic fingerprint sensor proposed in this chapter at a condition where the finger is first immersed into water and then dried with tissue paper.

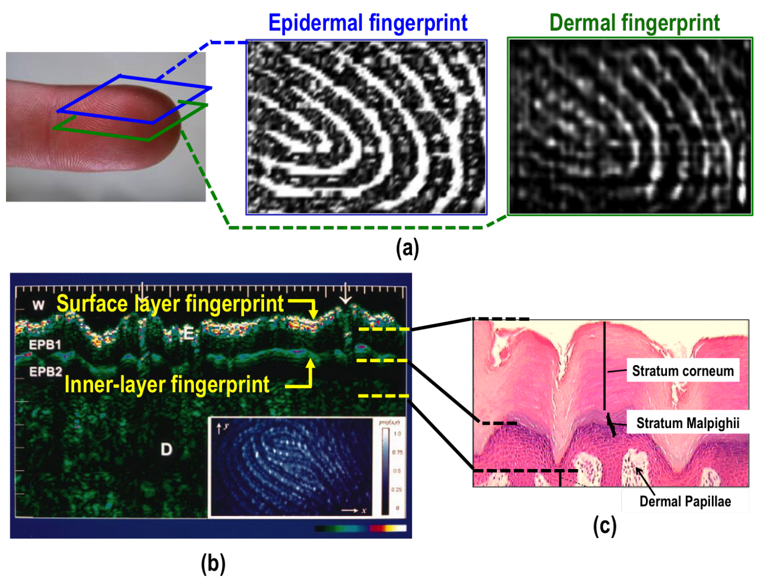

Figure 5.2: (a) Epidermal and dermal fingerprint captured with the ultrasonic fingerprint sensor in this work (b) a high-resolution ultrasound sonograph of a human fingertip in [32] and (c) anatomy cross-section of human fingertip [38].

benefits: First, the dermal image can provide information for verification for individuals with compromised epidermal fingerprint quality due to genetics or physical damage. Second, the sensor is robust to spoofing attacks with fingerprint phantoms that are not multi-layered like a real human fingerprint.

Presently available ultrasonic fingerprint sensors rely on piezoceramic transducers and mechanical scanning [33] and are too large for incorporation in consumer devices such as smart phones. Several attempts to miniaturization have been published. Reference [34] describes a first attempt toward miniaturization. An ultrasonic fingerprint sensor consisting of a control ASIC and a separate bulk-piezo pillar array is proposed to eliminate the need for mechanical scanning. However, the low bandwidth of the bulk-piezo pillar array prevents the sensor from performing pulse-echo imaging and it is therefore not suitable to image the dermal fingerprint.

Micromachining enables both miniaturization and the high fractional bandwidth required for high-resolution imaging at a distance from the sensor surface [6, 7]. A recent result [35] using a capacitive micro-machined ultrasonic transducer (CMUT) 2D array successfully demonstrates pulse-echo imaging of a fingerprint. A drawback of CMUT is the need for high-voltage drive voltages on the order of 100 V that require special circuit technologies and increase power dissipation.

In this chapter, we propose a fully-integrated ultrasonic fingerprint sensor-on-a-chip [36] realized by wafer-bonding MEMS and CMOS wafers to achieve compact size, high signal fidelity and low power consumption. Utilizing a Piezoelectric Micro-machined Ultrasonic Transducer (PMUT) array significantly lowers the driving voltage requirements to 24 V and enables high speed operation at up to 380 frames per second, enabling continuous identification in high-security applications. A low-power mode consuming only 10 μW allows the device to double as "power switch".

5.2 Ultrasonic Fingerprint Sensor

This section describes the finger anatomy and the operating principle of the sensor which motivate the architecture of the fingerprint sensor described in the next section. The acoustic physics background could be found in chapter 2.

Fingerprint and Finger Anatomy

The finger surface consists of ridges and valleys that form a fingerprint [37]. As shown in Fig. 5.2c, the texture of a fingerprint is essentially the extension of the dermal papillae, a small, nipple-like interdigitations of the dermis into the epidermis. The epidermis consists of several layers and they all run approximately parallel to the surface fingerprint pattern. As shown in Fig. 5.2c, the outer-most layer is called *stratum corneum*, comprising a layer of dead cells follows with a thin layer called stratum malpighii [38]. The impedance mismatch between stratum corneum and stratum malpighii results in echo-rich lines and forms the dermal fingerprint shown in Fig. 5.2b. In the proposed sensor, we mainly detect surface echoes (epidermal fingerprint) as well as this hidden inner-layer (dermal) fingerprint. Consequently, even if the surface fingerprint is contaminated or laminated, the dermal fingerprint remains intact and can be detected by an ultrasonic fingerprint sensor.

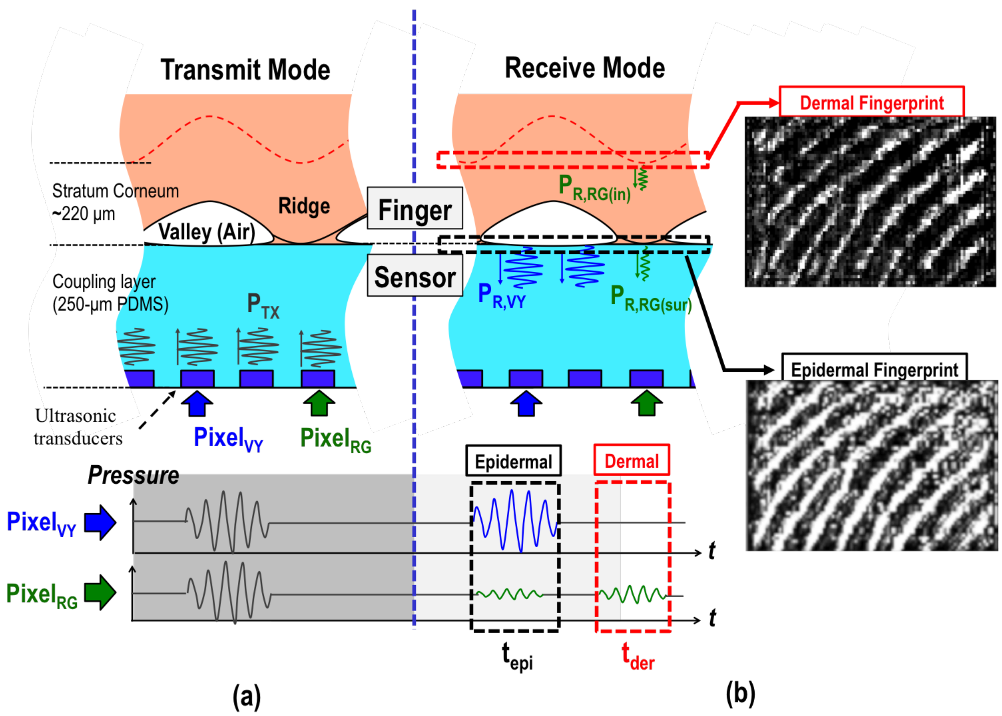

Figure 5.3: Operation of the sensor in (a) transmit and (b) receive mode

Ultrasonic Fingerprint Sensor Operating Principle

Fig. 5.3 shows the conceptual diagram of a finger put on top of an ultrasonic fingerprint sensor, which consists of an ultrasonic transducer array and a coupling layer. In this work, Polydimethylsiloxane (PDMS) is used as the coupling layer for its acoustic impedance $Z_{\mathrm{PDMS}} \sim 1.5$ MRayl, which is close to that of skin and water. At the boundary between the coupling media and the finger, the air inside valleys with acoustic impedance $Z_{vy} = Z_{\mathrm{air}} = 430$ Rayl have a huge impedance mismatch with PDMS, resulting in a strong reflection of nearly 100%. By contrast, the impedance of ridges, $Z_{rg} = Z_{\mathrm{tissue}} \sim 1.5\,\mathrm{MRayl}$ [39], is close to Z_{PDMS}, thus resulting in only a weak echo $P_{\mathrm{R,RG(sur)}}$. The wave at fingerprint ridges thus moves forward into finger until it hits the boundary between stratum corneum and stratum malpighii where again a strong reflection $P_{\mathrm{R,RG(in)}}$is generated due to impedance mismatch.

The reflected waves travel back to transducers. The inner-finger dermal echoes arrive at the sensor later than the surface echoes due to longer propagation distance. Hence by properly time-gating the received echoes, either the epidermal or dermal fingerprint can be imaged as shown in Fig. 5.3.

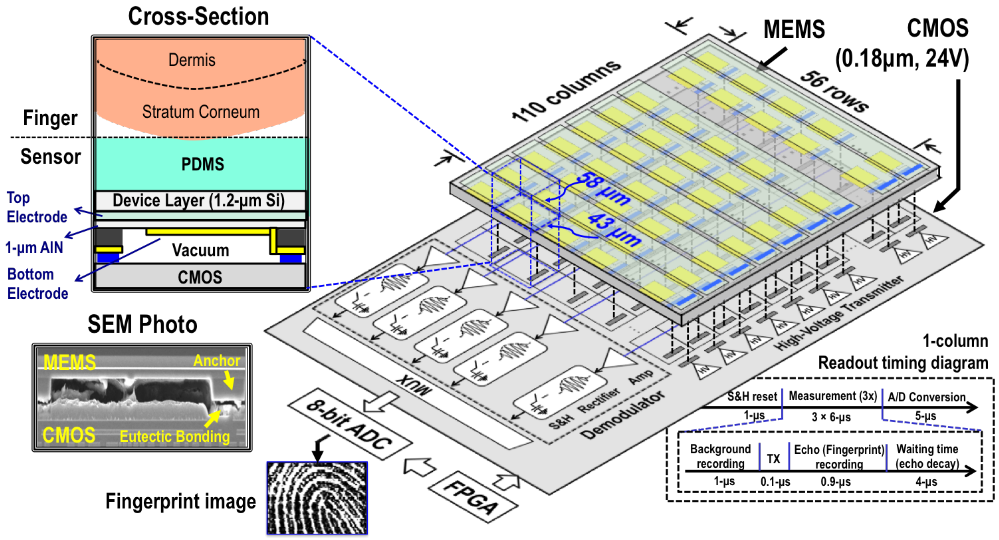

Figure 5.4: 3-D rendering of the fingerprint sensor comprising a MEMS wafer with the PMUTs and electronics wafer. The subsystems are bonded at the wafer level. For clarity, parts of the MEMS wafer without PMUTs are omitted from the drawing.

5.3 Sensor Architecture

Overview

Fig. 5.4 shows a 3-D prospective diagram of the sensor and electronics with the coupling layer (PDMS) omitted. It comprises a MEMS array with AlN transducers [40] and a custom readout interface fabricated in a 180 nm CMOS process with a 24 V HV transistor option. The transducers and circuits are fabricated on separated wafers. Each MEMS die comprises of 110×56 rectangular piezoelectric micromachined ultrasonic transducers (PMUTs) with a 43 and 58 μm pitch, corresponding to 582 and 431 dpi resolution, respectively, and is covered by a 250 μm PDMS [41] layer as coupling layer. The FPGA controller, ADC [42], and 24-V generation are off-chip.

The MEMS and CMOS wafers are eutetic bonded [43]. The anchor in each sensing element provides both mechanical support and electrical connection to the front-end electronics on the ASIC. The top-electrodes of the 56 transducers in one column are connected to shared high-voltage driver located at the edge of the ASIC.

On the receive side, directly digitizing the raw data from over 6000 pixels would consume excessive power. Thus, signal demodulating is performed in analog domain on-chip. Since the readout is column-sequential, all pixels in a row share one demodulator. The demodulator outputs are held by a S/H and read out through a MUX for off-chip digitization. An Opal Kelly FPGA [44] provides the digital control and data transfer between the ADC and the computer.

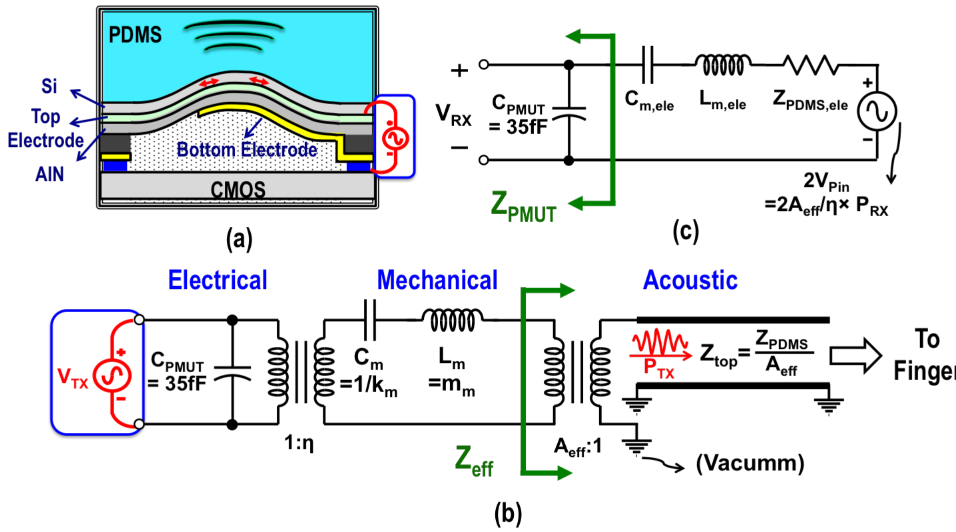

Figure 5.5: (a) PMUT cross-section, (b) electrical-mechanical-acoustic circuit model for the PMUT and (c) simplified PMUT model in receive mode.

Sensor Pixel: Piezoelectric Micro-machined Ultrasonic Transducer

Fig. 5.5a shows the operation of PMUT. A voltage applied across the AlN layer results in transverse stress, causing the membrane to buckle. Similarly, an incident pressure wave deflects the membrane resulting in a charge across the transducer.

Fig. 5.5b shows the electrical-mechanical-acoustic model of the PMUT [45]. The shunt parasitic capacitance $C_{\text{PMUT}} = 35\text{fF}$ is dominated by the overlap of the top and bottom electrodes. The first transformer with the ratio $\eta_1 = \eta = 0.78\,\mu\text{N/V}$ models the piezoelectric effect that converts the applied voltage to mechanical force. The PMUT membrane is modeled as an equivalent LC network with the membrane stiffness $k_m = 0.17\,\text{N}/\mu\text{m}$ and mass $m_m = 22\,\text{ng}$, respectively, corresponding to a resonant frequency of 14 MHz. A resistor can be added to model the anchor loss but is generally negligible and thus omitted in the diagram.

The second transformer accounts for the energy loss from the membrane vibration into the surrounding media as an acoustic wave, and its ratio is $\eta_2 = \frac{1}{A_{\text{eff}}}$, where A_{eff} is the effective area of PMUT. When driven, the membrane deflects with a parabolic shape, generating a nonuniform pressure wave with peak pressure P_{peak}. For this application, it is approximated with suffcient accuracy by a piston with area $A_{\text{eff}} = (1/3)A_{\text{PMUT}} = 460\,\mu\text{m}^2$ [46] and a uniform pressure P_{out}. The transmission lines represent the media above and below PMUT. Since the space between the MEMS and CMOS wafer is vacuum, the acoustic impedance $Z_{\text{bot}} = 0$ and $Z_{\text{top}} = Z_{\text{PDMS}}/A_{\text{eff}}$ ensures the entire acoustic energy is emitted in the direction of the finger, as desired.

The large acoustic impedance of PDMS transforms into a big equivalent series resistance

Z_{eff} in the mechanical domain, which results in low quality factor ~ 3 of the resonator that is suitable for sending short pulses. When driven at resonance, the L_m and C_m cancel out. The transmitting coefficient at resonance can hence be written as:

$$\eta_{\text{TX}} = \frac{P_{\text{TX}}}{V_{\text{TX}}} \approx \frac{\eta}{A_{\text{eff}}} \tag{5.1}$$

Fig. 5.5c shows the simplified model in receive mode with all components mapped to the electrical domain. The pressure source and the termination resistor at the right account for the power source that models pressure waves incident to PMUT. Again at resonance, $L_{\text{m,ele}}$ and $C_{\text{m,ele}}$ cancel out, and the equivalent (capacitive) input impedance $Z_{PMUT} = 324k\Omega$ resulting from C_{PMUT} generates an impedance mismatch between Z_{PMUT} and $Z_{\text{PDMS,ele}} \approx 100\text{M}\Omega$. Due to the voltage divider between Z_{PMUT} and $Z_{\text{PDMS,ele}}$, only $\approx 0.3\%$ of the received pressure signal is converted to voltage. The receiver sensitivity is therefore:

$$\eta_{\text{RX}} = \frac{V_{\text{RX}}}{P_{\text{RX}}} \approx 2\frac{Z_{\text{PMUT}}}{Z_{\text{PDMS}}}\frac{A_{\text{eff}}}{\eta} \approx 344\mu\text{V/kPa} \tag{5.2}$$

Beam-forming

Since the PMUT is a resonator that filters the pressure signal, driver linearity is not important. Consequently, a two-level driver (0 and 24V) is used for good efficiency and to minimize circuit complexity. The amplitude of output pressure of the transducer is

$$P_{\text{TX}} = \frac{\eta V_{\text{TX}}}{A_{\text{eff}}}(1 - e^{-\omega_B t}) \tag{5.3}$$

where $\omega_B = (2\pi)4\,\text{MHz}$ is the radial bandwidth.

The equation suggests that a burst-time $t = T_{TX} \sim Q/f_0$ is sufficient to reach 99% of its maximum amplitude. Hence, upon triggering, 3-cycles of 24 V square wave at 14 MHz are applied to each column of the PMUT array. Note that the extra driving cycle does not increase output pressure but lengthens the pulse-width, thereby lowering the depth resolution. Also, despite mismatch present among individual PMUT elements due to a large die-size, large bandwidth of PMUT makes it insensitive to frequency mismatch thus permitting the entire array to be driven at the same frequency.

After the end of the transmit cycle, the stored mechanical energy in the transducer dissipates as the transducer rings down at the resonant frequency [47]. Assuming the transducer is excited to full amplitude at $f_0 = 14\,\text{MHz}$, the ring-down pressure amplitude is:

$$P_{\text{TX}} = \frac{\eta V_{\text{TX}}}{A_{\text{eff}}}u(t - T_{\text{TX}})e^{-\omega_B(t - T_{\text{TX}})} \tag{5.4}$$

This transducer ring-down can induce a dead-zone in the system and this will be further discussed in the ASIC design section.

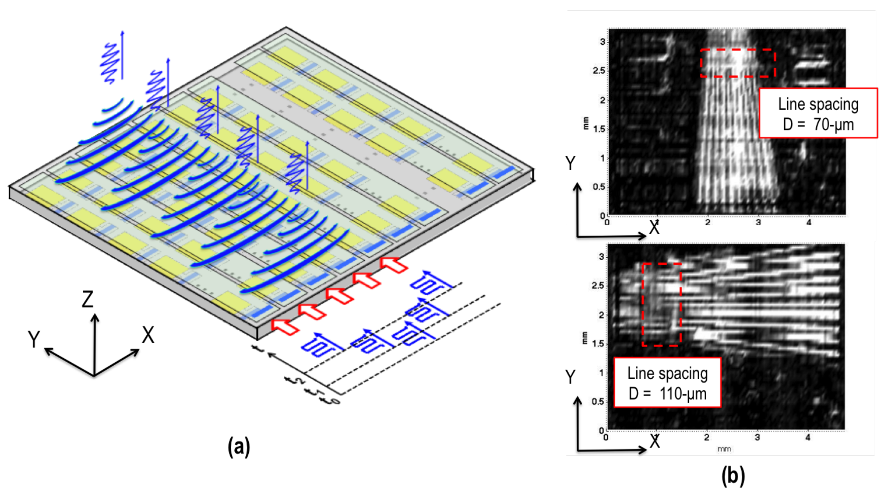

Figure 5.6: (a) Conceptual diagram showing X-direction beam-forming on the device and (b) resolution measurement with phantom from NIST [48].

To further increase power and focus, four adjacent columns are excited with specific delays adjusted to focus the beam in one dimension. As shown in Fig. 5.6, the delay to the channels is assigned such that the wave generated by each column arrives at the same time over the center column of the group at the top of the 250 μm thick PDMS layer to produce constructive interference. This generates a focused pressure wave with 15 kPa amplitude and 120 μm beamwidth. Since the beam-forming technique is only applied to the X-direction, the imaging resolution of the device is superior at the X-direction. Fig. 5.6b shows the imaging result with a standard resolution test from the National Institute of Standards and Technology (NIST) [48] using a PDMS test phantom. The result indicates an imaging resolution of 70 μm and 110 μm in the X and Y direction, respectively.

Received Signal

The ultrasonic wave transmitted towards a finger experiences both attenuation and spreading loss. The round-trip loss inside the 250 μm thick PDMS is ~15 dB. Therefore, for the pixel under a valley, despite total reflection at the boundary between PDMS and a valley (air), the amplitude of the wave that reaches PMUT reduces from 15 kPa to 2.5 kPa, which translates to ~860 μV at the input of the readout amplifiers.

On the other hand, for the pixel under a ridge, ideally no reflection occurs at the PDMS-finger boundary and the wave travels into the finger to be reflected by the stratum corneum-malpighii interface. This wave experiences attenuation from both PDMS and finger tissue. Besides, the interface only partially reflects the wave. The resulting overall loss is ~23 dB from the incident wave and ~800 Pa of pressure accounting for the dermal ridge reflection to reach the pixel, corresponding to 340 μV at the transducer output.

The two signals from surface-valley and inner-ridge are separated in time by ~300 ns.

Although the two signal won't overlap on one pixel, the PMUT is designed to be able to separate the echoes in time-domain, thus permitting a shared time-gating window by the entire array for imaging the epidermal or dermal fingerprint. With the speed of sound of the media equal to v, it can be shown that for a pulse that is shaped by a second order transducer response on transmission and reception, and assuming that the amplitude between the two pulses must fall to half the maximum level in order to resolve the two targets, the depth resolution Δd along the axis is: [49]

$$\Delta d = (v/2)(T_{TX} + (0.27/BW)) \tag{5.5}$$

Assuming the speed of sound of 1500 m/s in human body, eq. 5.5 suggests that our device has a resolution of ~210 μm in finger, sufficient to resolve the two echoes from epidermis and dermal-layer separated by ~230 μm thick stratum corneum layer.

Measurement Cycle Overview

Readout is column-sequential and begins with a reset phase during which the data in the demodulator from the previous column measurement is cleared and the digital circuits are initialized. The bottom-right of Fig. 5.4 shows a timing diagram of one column measurement: Imaging starts by first recording the background image of the column by sampling the signal as the HV driver disables. Subsequently, all 56 transducers in the selected column are excited with three 24 V pulses at 14 MHz, producing an ultrasonic pulse towards a finger for pulse-echo measurement.

After the measurement, the emitted ultrasonic wave bounces back-and-forth inside the PDMS. A 4 μs delay is employed to ensure that echoes are attenuated below the noise floor. The readout sequence is then repeated for a total of three times to improve the SNR. The final 5 μs of the column readout is allocated for AD conversion. The full readout sequence takes 24 μs per column and 2.64 ms for the entire array (110 columns), translating into a maximum output rate of 380 fps. The high operating speed can potentially enable continuous verification for high-security applications (e.g., by incorporating fingerprint recognizers into the keys of a keyboard).

5.4 Fingerprint Readout ASIC Design

Interfacing HV and LV Electronics with PMUT

The low conversion ratio of ultrasonic transducers motivates an efficient design of high-voltage driving pulser. However, HV transistors are accompanied with parasitics that can be several pF, resulting in significant attenuation [50]. Since the shunt capacitance of each PMUT is only 35 fF, even a shunt parasitic capacitance of 1 pF attenuates the signal by ~ 30× due to charge sharing.

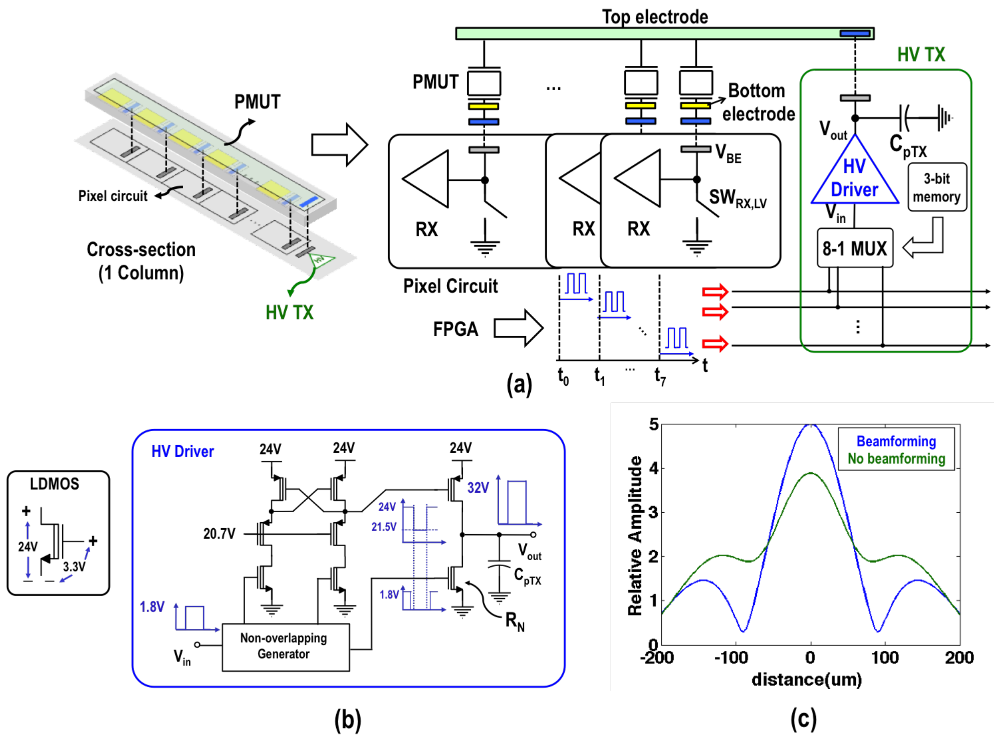

Figure 5.7: (a) Simplified diagram of the driving and readout electronics for one column. (b) High-voltage driver circuit. (c) Transducer amplitude with and without beam forming (simulation).

Operating PMUT as a 2-port device that separates the driving (high-voltage) and receiving (low-voltage) port avoids this attenuation [45]. Shown in Fig. 5.7a, the high-voltage driver is connected to the shared top electrodes of PMUT as the driving port while the bottom electrode is used for receiving. During the transmit phase, the bottom electrode of each PMUT in the column is grounded by the switch $SW_{\mathrm{RX,LV}}$ and thus at the receiving port, the front-end electronic is never exposed to the high voltage. The switch $SW_{\mathrm{RX,LV}}$ is realized with a low-voltage transistor with small parasitics.

During the receive phase, the top-electrode is grounded via the high-voltage driver and $SW_{\mathrm{TX,LV}}$ is opened. Since the parasitic capacitance from the high-voltage electronics C_{pTX} is effectively shorted, it does not result in signal attenuation.

High-Voltage Drivers

The high-voltage transistors in the process used for this work are LDMOS, which can withstand up to 24 V V_{DS} but only 3.3 V V_{GS}. Fig. 5.7b shows the circuit diagram of a high-voltage driver using a latch-based level-shifter with a voltage limiting switch to limit the gate swing on HVPMOS of the output stage to $HVV_{DD}-3.3\,\mathrm{V}+V_{\mathrm{TH,p}}(\approx 0.8\,\mathrm{V})$ [51]. The output buffer is sized to be able to drive the entire PMUT column with a total capacitance $\sim 2\,\mathrm{pF}$, with a maximum output current of $\sim 10\,\mathrm{mA}$ to ensure a 14 MHz 24 V rail-to-rail driving waveform. A non-overlapping waveform generator circuit separates the rising and falling edge of the gate-control on HVNMOS and HVPMOS, thus eliminating the crowbar current and resulting power dissipation during the switching transients as shown in Fig. 5.7b.

The output parasitic capacitance of the HV driver C_{pTX} is $\sim$0.8 pF and the PMUT capacitance in a column is $\sim$2 pF. The overall driving efficiency defined as the ratio of the power delivered to the transducer to the power draw from the supplies is $\sim$ 40%. The loss is dominated by output parasitics and crow-bar current in level-shifter block. If a thick-oxide HVFET device is available in the process, a HV-driver structure, similar to the one proposed in [52], can be used to completely remove the crow-bar current and further increase driving efficiency. Also, since the PMUT itself acts as a second order filter, the high-frequency component of the square wave is filtered and wasted. Ideally, a linear driver as in [53] gives the best electrical-to-acoustic efficiency, but the static bias current flowing through HVV_{DD} to ground is highly undesired. A three-level HV pulser structure was proposed in [54] that consumes no static current and provides a good compensation between the rail-to-rail pulse driving and sinusoidal wave driving. However the bandwidth of the circuit is limited, and hence this solution is not suitable for this work.

Fig. 5.7c shows the simulated 5-column beam-forming beam pattern at the lateral (X) direction with ideal timing versus 5 ns delay resolution, which is limited by external FPGA control. Simulation result shows $\sim$35% of pressure increase compared to the case without beam-forming.

The bottom electrode is connected to ground via $SW_{\mathrm{RX,LV}}$ during the transmit cycle. The switch is sized to guarantee that the voltage on bottom electrode V_{BE} will not exceed 2 V upon the rising edge of the driving pulse. With the HVPMOS in the driver sized to have an on-resistance of $2\,\mathrm{k\Omega}$ at 24 V V_{SD} (which is $\sim 110\,\mathrm{k\Omega}$ for 1 of the 56 pixels in a column), $SW_{\mathrm{RX,LV}}$ is sized to have an on-resistance less than $10\,\mathrm{k\Omega}$.

In receive mode, the top-electrodes of the PMUTs in a column are grounded via the output HVNMOS in one HV-driver. The effective resistance R_N of HVNMOS at 0 V_{DS} that is shared by all the 56 PMUTs is designed to be much smaller than the PMUT impedance at resonance $\sim 324\,\mathrm{k\Omega}$ in order to avoid further attenuating the signal. In this design, R_N is sized $\sim 28\,\Omega$ (which is equivalently $\sim 1.57\,\mathrm{k\Omega}$ to one of the 56 PMUTs) to ensure that the attenuation from the signal is less than 0.5%. This leads to a large HVNMOS size that dominates the output parasitics C_{pTX} and the die area of the HV driver.

Receiver Front-End

Fig. 5.8 shows an overview and detail of the pixel readout circuits for one of 56 identical rows. To reduce cross-talk, a differential architecture is adopted that pairs the selected PMUT pixel with a replica at the edge of the array. The replicas have the same parasitics,

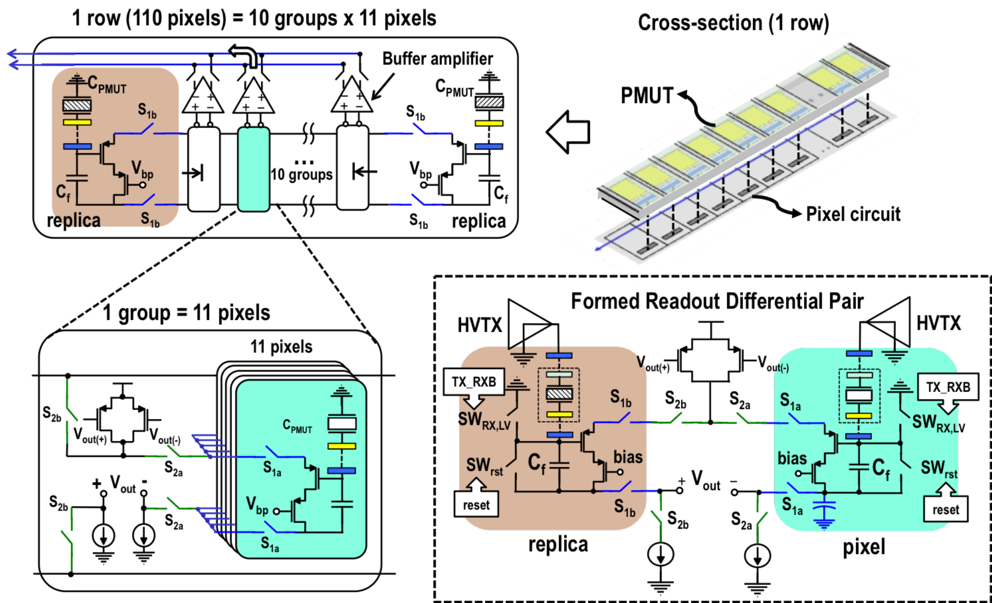

Figure 5.8: Circuit diagram of the pixel readout circuit for one of 56 identical rows

but are not mechanically released and hence are insensitive to acoustic inputs. To form a differential pair, a direct muxing from the replica to the 110 PMUTs in a row can be used, but that results in large capacitive loading due to 110 switches connected to the pixels. Instead, the pixels in a row are divided into ten groups with eleven pixels each. Switches S_{1a} select the pixel, S_{1b} the replica at the edge of the array that is closest to the selected pixel, and S_{2b} the group. S_{2a} is used to balance the load on either side of the differential pair, consisting of ten S_{2b} and two S_{1b} on the left side of the differential pair and eleven S_{1a} and one S_{2a} on the right, respectively. The current source loads are shared by all pixels in a group. Finally, common-mode feedback is accomplished by connecting the output voltage to the top two transistors.

Upon switching from transmit mode to receive mode, reset signal removes the charge on the feedback capacitor C_f and sets the bias point of the front-end. However, the system has a dead-zone due to ring-down from the transducer. As illustrated in Fig. 5.9, after the end of the transmit cycle, the stored mechanical energy in the transducer dissipates as the transducer rings down at the resonant frequency, which results in a large signal appearing at the electrical port of PMUT that can overlap with the received signal if the reflected signal comes at the same time. Based on eq. 5.2 and eq. 5.4, the ring-down voltage signal at the electrical port is:

$$V_{ring} = 2V_{TX}\frac{Z_{PMUT}}{Z_{PDMS}}u(t-T_{TX})e^{-\omega_B(t-T_{TX})}cos(\omega_0 t) \tag{5.6}$$

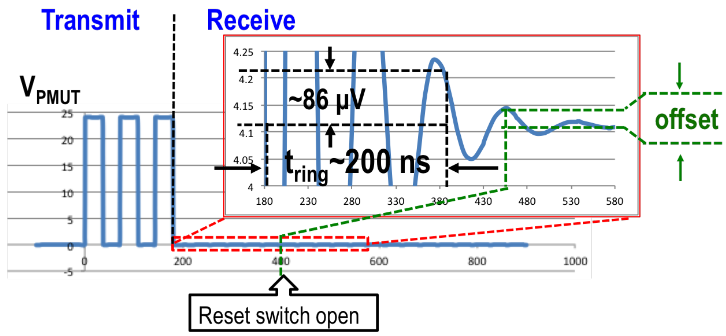

Figure 5.9: PMUT voltage while actively driven and during mechanical ring-down (simulation).

where Z_{PMUT} ~324 kΩ is the impedance of PMUT capacitance, C_{PMUT}, R_{PDMS} =1.06 GΩ is the equivalent motional impedance for PDMS seen from the electrical port. A delay of ~170 ns reduces this ringdown to ~86 μV, well below the received signal.

Fig. 5.9 shows the simulation result from three 24 V 14 MHz pulses at its electrical port and then disconnecting the driver immediately to the PMUT model in Fig. 5.5, verifying the delay calculated above. The ring-down signal gives a design value for the thickness of the coupling materials. Assuming the speed of sound v = 1000 m/s in PDMS, the minimum detectable distance d_{min} is therefore $d_{\text{min}} = v \times (t_{\text{ring}} + T_{\text{TX}})/2$ =190 μm, indicating that at least 190 μm of PDMS needs to be placed on top of the PMUT to delay the first returning echo such that it will not fall into the dead-zone of the sensor. In this prototype, a 250 μm thick PDMS layer is used to guarantee the ring-down and first-echo are well-separated.

The ring-down signal also affects the design of reset switch timing. If the reset switch is opened too early, the front-end can record the ringdown signal and define it as AC ground of the front-end. After the PMUT stops bouncing and becomes silent, unwanted offset appears. Fig. 5.9 shows the amplitude the recorded ringing signal when the switch opens. In this prototype, the reset switch is kept closed for an extra 100 ns in addition to the 200 ns ringdown time to reduce this unwanted offset.

The size of the feedback capacitor C_f is approximately equal to the capacitance of the transducer (35 fF), which results in unity gain. Ideally, the feedback capacitor can be designed smaller than C_{PMUT} to achieve larger gain and better noise performance over the receiver chain, but in this design the capacitor size is limited by the design rule.

Receiver Gain-Chain

Fig. 5.10 shows the block diagram of the overall receiver chain. The output of the front-end is amplified by the buffer circuit with gain ~10 dB and is shared in a group. The output of the front-end buffer is passed to another 2 closed-loop amplifiers with 12 dB gain each inside the demodulator block and therefore are shared by the pixels in a row. The input referred

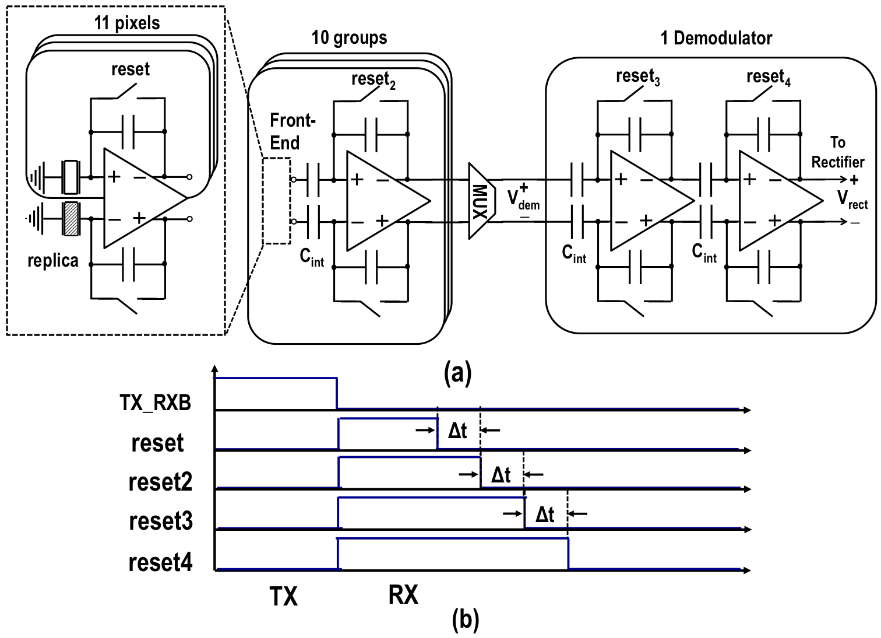

Figure 5.10: (a) Block diagram of the receiver gain-chain. (b) Timing diagram of the reset of the receiver gain stages.

noise is thus dominated by both the front-end amplifier and the buffer circuit. Including the noise contribution from gain-chain after the front-end, input-referred integrated noise is $46\,\mu$V, which is $\sim$18 dB smaller than the smallest signal we expected: the inner-finger ridge echo $340\,\mu$V.

Fig. 5.10b shows the reset control applied to each stage. The reset switches of each amplifier are turned off successively with a delay Δt =10 ns after the reset signal for the front-end to store the offset coming from each stage on the inter-stage coupling capacitors C_{int}.

The 3-dB corner frequency of the amplifier in each stage is designed at 20 MHz to reduce the noise above 20 MHz and thus reduce the noise folded into the base-band at demodulation.

Fingerprint Imaging

Ideally the finger topology would be extracted from the arrival times of the echoes from the various layers at the surface and inside the finger. Unfortunately the corresponding algorithms are rather complex and best implemented with digital circuitry. Instead, an analog approach that exploits both arrival time and amplitude of the received echoes has been chosen in this realization.

Fig. 5.11 shows the concept. After amplification, an envelope detector extracts the amplitude from the received signal. The output is captured by a sample-and-hold circuit

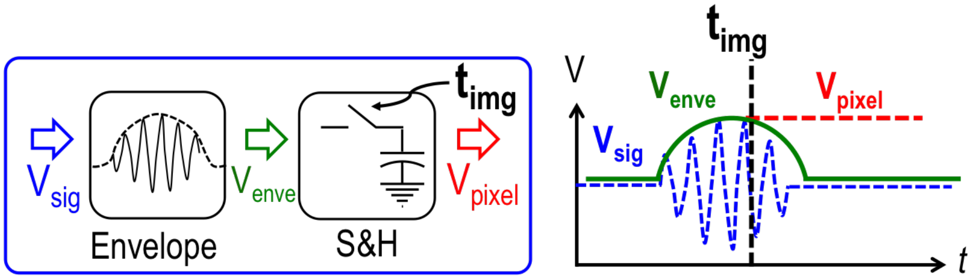

Figure 5.11: Demodulator that converts timing to amplitude information for reduced readout complexity.

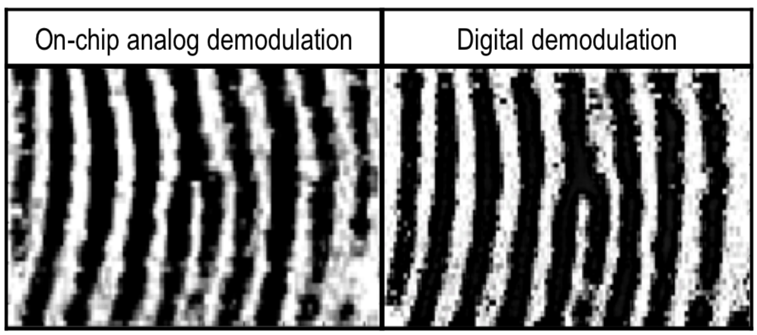

Figure 5.12: Comparison of image quality using the on-chip amplitude based analog demodulator (left) with external digital demodulation based on time-of-flight (right).

at an appropriately chosen time t_{img}. Near the target depth set by t_{img}, the amplitude of the envelope has been found to be a good proxy for depth, thus minimizing the number of images that need to be taken to extract the full 3-D representation of the finger.

Fig. 5.12 compares the image quality of this solution with a digital post-processor that reconstructs the image from the time of arrival of the echoes. Since the latter solution requires digitization of the entire ac waveforms from all pixels, image acquisition is much slower. The difference in quality from the two techniques is acceptable and represents a good compromise reducing circuit complexity and power dissipation.

In practice, only two image need to be taken to extract relevant information from the surface fingerprint and the inner layer of the finger. For the first image, t_{img} is set to correspond to the surface of the sensor. A small offset is applied to eliminate ambiguity between amplitude and depth resulting from the symmetry of the envelope. Since valleys generate a strong echo and echoes from inside the finger arrive later, good contrast is obtained.

Ridges generate echoes from the stratum corneum inside the finger. Since the thickness of this layers varies by about 70 μm between individuals [32], the sampling time is adjusted for different users. Since the correct timing can be established from imaging only a few

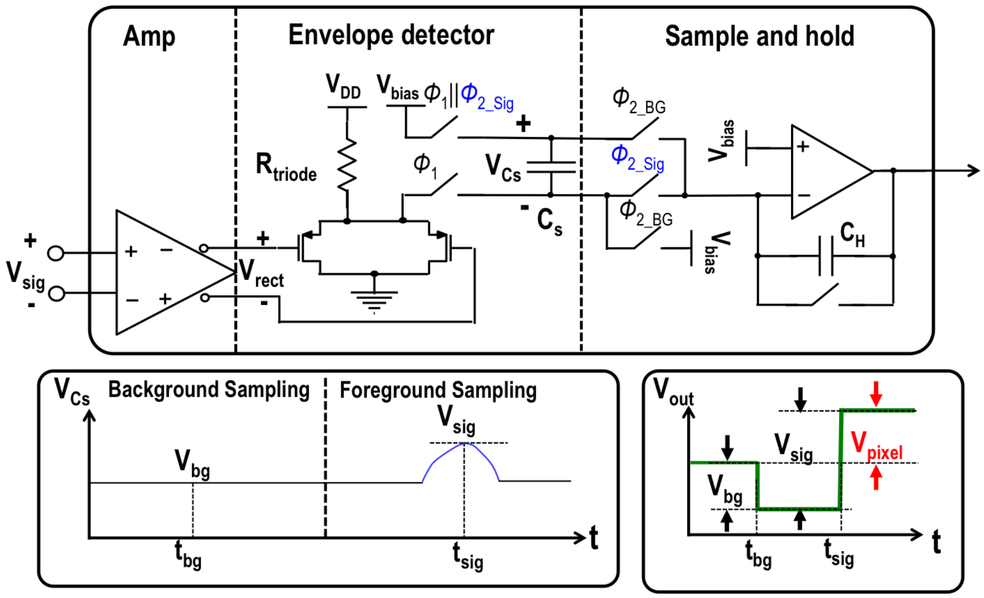

Figure 5.13: Circuit diagram of the demodulator

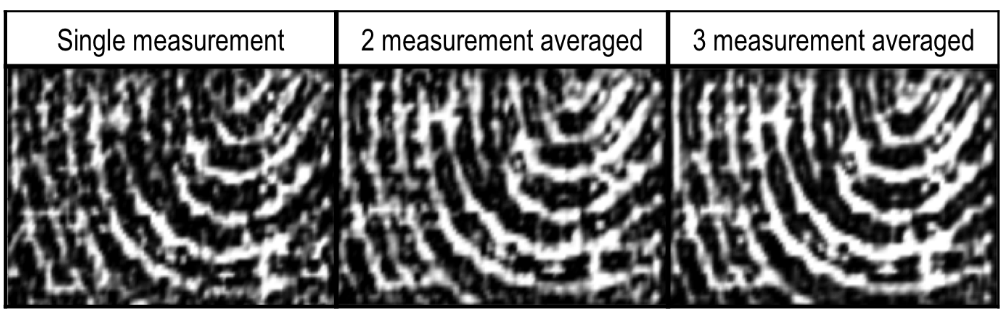

Figure 5.14: Fingerprint image quality as a function of the number of images averaged. The readout times for 1 to 3 frames are 1.32, 1.98, and 2.64 μs, respectively.

columns of the entire finger, this adjustment adds a negligible penalty to the time required to acquire a 3-D fingerprint image.

Fig. 5.13 shows the circuit implementation of the demodulator which combines a rectifier with differential-to-single-ended conversion and sample-and-hold circuit. Correlated double sampling (CDS) is used to reject offset and kT/C noise from the preamplifiers. The rectifier consists of a source follower with low-pass filtering at the output realized by capacitor C_s and resistor R_{triode} [55]. The latter is implemented with a MOSFET biased in the linear region. The filter corner is at 10 MHz.

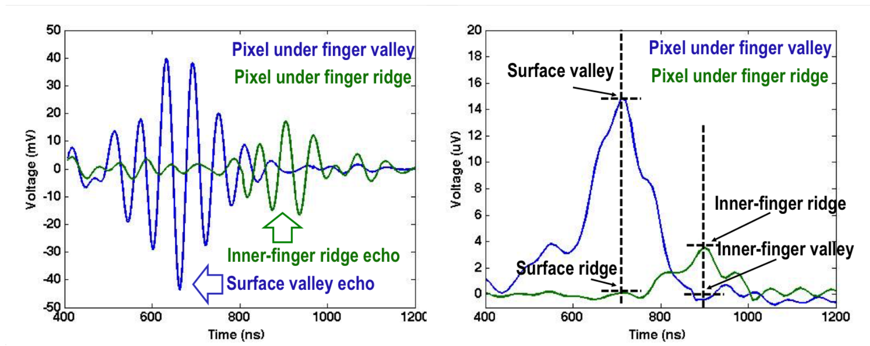

Figure 5.15: Fingerprint echoes before and after demodulation.

The output from several images is summed on C_H to improve image quality. Fig. 5.14 shows images with one, two and three averages. With single measurement the fingerprint pattern is slightly vague especially at the edge of the array, and the valley and ridge lines of fingerprint also slightly wiggles. The quality improve as we average more images, and finally an average of three gives a good compromise between image quality and frame rate that is 380 fps in this work.

5.5 Measurement Results

The fingerprint sensor is evaluated both at the circuit level by examining the detailed waveforms of received echoes, and as an imager of both phantoms and real fingers. The effect of moisture on image quality and rejection of false fingers are also discussed.

Fig. 5.15 shows the received echoes before and after demodulation. As expected, echoes from the surface and inner finger are separated in time by approximately 200 ns but show some overlap due to finite sensor bandwidth. The amplitude of the echo from inside the finger is almost five times smaller as a result of additional attenuation, beam spreading, and a smaller impedance mismatch than at the PDMS-finger valley (air) interface. This translates into a contrast of 20:1 at the finger surface and 3:1 for echoes from inside the finger.

The 3-D imaging capability has been evaluated with a phantom fabricated from two layers of 125 μm thick PDMS sheets with patterns engraved with the laser cutter. The layer thickness is about half of the depth of the dermal finger image to account for the different velocity of sound in PDMS and tissue. The pattern at the surface of the phantom consists of diagonal lines with 750 μm pitch while the "Cal" logo has been engraved on the second sheet. Fig. 5.16 shows a cross-section and optical rendering of the semitransparent phantom, and images recorded with the fingerprint sensor with the timing set for the surface and inner layer. The "Cal" logo is partially obscured by the diagonal lines on the surface of the phantom.

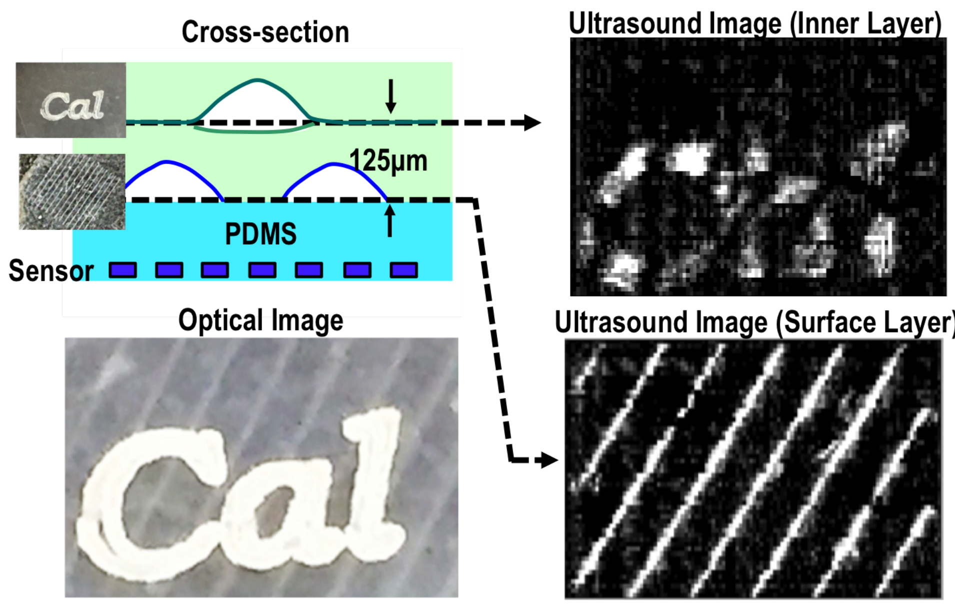

Figure 5.16: 3D images of a 2-layer PDMS phantom.

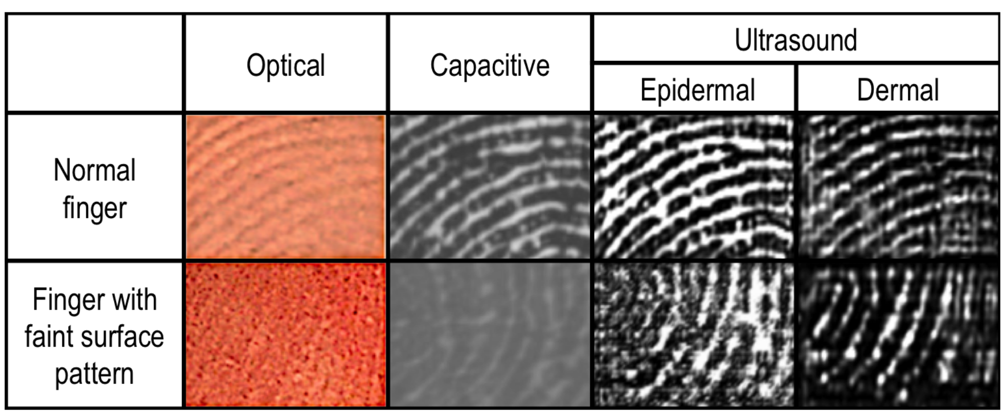

Figure 5.17: Fingerprints captured with an optical, capacitive, and the ultrasonic sensor presented in this work.

Fig. 5.17 shows images recorded from a normal finger, and a finger exhibiting only a faint pattern on its surface. Faint patterns occur for a subset of the population for genetic reasons or chemical or mechanical abrasion. The optical and capacitive image, taken with commercial sensors, show significant degradation for the faint finger surface pattern. The ultrasonic epidermal image also shows degradation, but much of the information is still available in the dermal print and can be used for verification. The dermal and epidermal images are strongly correlated and approximately complementary because of the blocking of

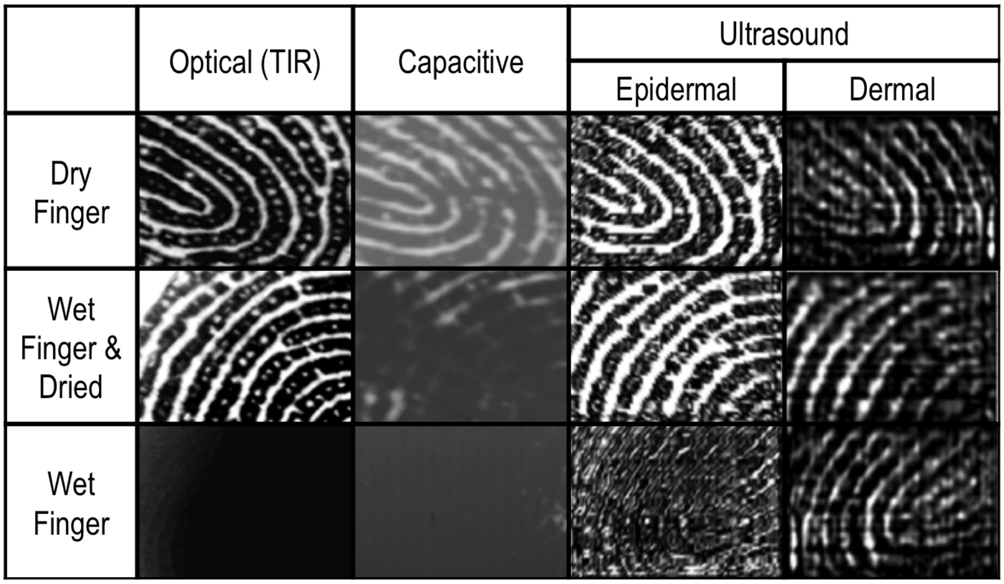

Figure 5.18: Fingerprint captured with commercial optical and capacitive fingerprint sensor comparing with the image captured with the proposed ultrasound fingerprint sensor for different conditions of finger wetness.

ultrasound at finger valleys.

Capacitive fingerprint sensors suffer from performance degradation in the presence of moisture due to the high permittivity of water that is comparable to that of tissue. Fig. 5.18 shows optical, capacitive, and ultrasound images for dry and wet fingers, as well as wet fingers that have been dried with a tissue to simulate the process of hand-washing. The optical image, taken by a commercial TIR (Total Internal Reflection) imagers copes well with a humid finger, but the image disappears for a completely wet finger because of the similarity of the optical refraction index of water and tissue. By contrast, the capacitive fingerprint sensor quality suffers even from modest moisture. For the ultrasonic sensor degradation is observed only for surface images of very wet fingers where the valleys are substantially filled with water. Even in this case, the fingerprint image is contained in the dermal image. This suggest that ultrasonic fingerprint imagers are significantly less sensitive to humidity than either capacitive or optical solutions.

Fig. 5.19 simulates the situation where the sensor is presented with a finger phantom, constructed in this case from a PDMS sheet with information obtained from an optical fingerprint image. Since the optical image (for example extracted from a fingerprint recovered from the glass surface of a smartphone) renders only surface information, the phantom is 2-D only and does not contain the 3-D information present in real fingers. Unlike either optical or capacitive sensors, the ultrasonic fingerprint sensor readily distinguishes the real from the phantom finger with the dermal image completely absent from the phantom. The

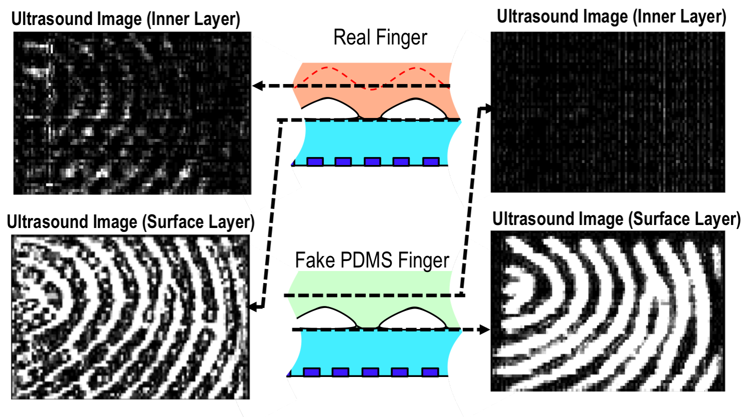

Figure 5.19: Ultrasound images from a real finger versus those obtained from a PDMS mock-up. Both the epidermal and dermal images are easily recognizable as fakes.

surface image also contains additional detail such as sweat pores that cannot be recovered by low quality surface fingerprints, such as those left by sweat or oil.

Since 3-D fingerprint information is difficult to obtain without e.g. a sensor such as the one presented here, the ability of the ultrasonic fingerprint sensor to reject 2-D only phantoms represents a significant enhancement of security over optical and capacitive techniques. Even if 3-D information were available, the phantom would need to be fabricated from materials with similar acoustic properties as real tissue to be accepted by the detector.

Fingerprint readout takes 24 μs per column, or 2.64 ms for an entire frame, corresponding to a maximum output rate of 380 fps that includes averaging three images. This rate decreases to 190 fps when both epidermal and dermal images are taking, still sufficient for applications such as on-line verification while typing on a keyboard.

The energy consumed is 2.5 μJ per column or 280 μJ for a complete image at one depth setting. Recording only select columns enables a low-power finger detection feature. Since the characteristic ridge-valley pattern can be extracted from single column images and is not present in other likely materials such as cloth or the leather of a purse where the device with the sensor may be stored, the fingerprint sensor can double as a low-power power switch: for example, a one-column finger-detect mode at four frames per second consumes only 10 μW static power, acceptable in many battery powered devices such as smart phones.

Table I compares this work with other published fingerprint sensors. It is the first compact implementation of a 3-D imagers with a form-factor that meets the requirements for inclusion in small hand-held devices and achieves higher detection rates and lower power dissipation than the other solutions. Finger presence is a further benefit that is not available in the other devices.

Fig. 5.20 shows a die shot of the ASIC before bonding to the MEMS wafer. The area is dominated by the imager pixel readout circuits in the center of the die occupying an area

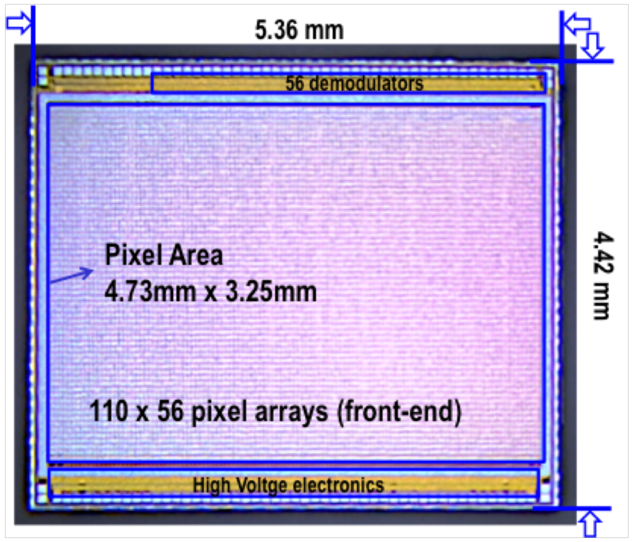

Figure 5.20: Die shot of the ASIC without the MEMS chip bonded.

Table II: Comparison of different fingerprint sensors

	This work	IUS' 04 [33]	Jsensor'10 [34]	ISSCC'08 [55]
Method	Ultrasonic (Pulse-Echo)	Ultrasonic (Impediography)	Ultrasonic (Pulse-Echo)	Capacitive
Process	0.18um CMOS + MEMS, wafer-bonded	Discrete electronics + MEMS	Discrete electronics + MEMS	0.5um CMOS
Imaging capability	3D image	2D image	3D image	2D image
Inner-finger Imaging	Yes	No	No	No
Transducer	PMUT	Bulk Piezo	CMUT	Capacitor
Array size	110 x 56 pixels 4.73 x 3.25 mm^2	64 x 64 pixels 8.06 x 8.06 mm^2	1 x 192 pixels 0.11 x 21.5mm^2	224 x 256 pixels 11.2 x 12.8 mm^2
Pixel size	43 x 58 μm^2 (591 x 438 dpi)	126 x 126 μm^2 (250 x 250 dpi)	112 x 112 μm^2 (227 x 227 dpi)	50 x 50 μm^2 (508 x 508 dpi)
Frame rate	380 frame/sec	50 frame/sec	N/A	N/A
Energy per measurement	280uJ	N/A	N/A	25mW÷ frame rate

of 4.73 by 3.24 mm^2, with rows at the top and bottom with the signal demodulators and high-voltage drivers, respectively. The chip has been fabricated in a 180 nm CMOS process with 24 V LDMOS high-voltage transistor and measures. The overall chip dimensions are 5.36 by 4.42 mm^2, corresponding to an imaging fill-factor of 65%.

5.6 Conclusion

A 3-D ultrasonic fingerprint sensor-on-a-chip is presented in this chapter. The use of PMUT transducers with customized ASIC bonded at wafer level minimizes the parasitics and reduces the system complexity. The sensor is resilient to humidity, and the capability of generating a three-dimensional, volumetric image of the finger surface and the tissues beneath the finger surface makes it extremely difficult to deceive the sensor with phantom. The sensor images a fingerprint within 2.64 ms and 280 μJ, and could be turned to a standby mode consuming 10 μW that only detects whether finger presents.

Chapter 6

Conclusion

The advent of small and inexpensive MEMS ultrasonic transducers combined with highly integrated electronic interfaces enables a host of new applications.

For example, blood pressure is an important biomarker for a range of cardio-vascular diseases. Unfortunately, although at-home monitors have been available for quite some time, these devices are quite inconvenient to use, resulting in very spotty monitoring for most individuals. A more convenient device that ideally could be used continually might uncover interesting correlations of blood pressure with life-style and other external factors and might lead to new treatment approaches. While ultrasound is not capable of directly measuring blood-pressure, some authors [58] have found correlation between pressure and the velocity of blood-flow obtained from ultrasound Doppler measurements. Should this correlation, possibly combined with other markers, prove out, it may enable the envisioned non-obtrusive, continual sensor.

Non-destructive testing (NDT) is another area that could benefit from smaller and lower-cost ultrasonic transducers. Ultrasound is already used to assess reduction of the wall-thickness of pipes due to corrosion, but their use is constrained by size, cost, and power-dissipation. It is conceivable that MEMS transducers combined with custom electronics could address these limitations.

The Neural Dust project [59] uses ultrasound for delivering power to implants, data communication, and to image the location of these implants inside the body. Compared to conventional hard-wired neural probes, the ultrasound solution is much less invasive and enables higher special density.

Bibliography

[1] Sonavation, “Next generation ultrasound biometric technology for secure authentication”, http://www.sonavation.com/, retrieved April 18, 2016

[2] D. T. Blackstock, Fundamentals of Physical Acoustics. NewYork, NY, USA: Wiley, 2000.

[3] N. M. Toole, “Basic physics of ultrasonographic imaging,” WHO Diagnostic Imaging Laboratory, 2005.

[4] American Piezo, “850 Navy II Physical and piezoelectric properties of APC material”, `https://www.americanpiezo.com/apc-materials/piezoelectric-properties.html`.

[5] D. R. Wagner, “Ultrasound as a tool to assess body fat,” *J. Obes.*, Jul. 2013.

[6] I. Ladabaum, X. Jin, H. T. Soh, A. Atalar and B. T. Khuri-Yakub, ”Surface micromachined capacitive ultrasonic transducers,” in *IEEE Transactions on Ultrasonics, Ferroelectrics, and Frequency Control*, vol. 45, no. 3, pp. 678-690, May 1998.

[7] P. Muralt *et al.*, ”Piezoelectric micromachined ultrasonic transducers based on PZT thin films,” in *IEEE Transactions on Ultrasonics, Ferroelectrics, and Frequency Control*, vol. 52, no. 12, pp. 2276-2288, Dec. 2005.

[8] Y. Lu, H-. Y Tang, S. Fung, B. E. Boser, D. A. Horsley, “Short-range and high-resolution ultrasound imaging using an 8 MHz aluminum nitride PMUT array,” *IEEE Int. Conf. on MEMS,*Micro Electro Mechanical Systems (MEMS), pp. 140-143, Jan. 2015.

[9] J.M. Tsai, M. Daneman, B. Boser, D. Horsley, M. Rais-Zadeh,H-Y. Tang, Y. Lu, O. Rozen, F. Liu, M. Lim, F. Assaderaghi, ”Versatile CMOS-MEMS integrated piezoelectric platform,” in *Solid-State Sensors, Actuators and Microsystems (TRANSDUCERS)*, 2015 Transducers - 2015 18th International Conference on , vol., no., pp.2248-2251, 21-25 June 2015

[10] A. Logan, J.T.W. Yeow, ”Fabricating capacitive micromachined ultrasonic transducers with a novel silicon-nitride-Based wafer bonding process,” in *Ultrasonics, Ferroelectrics, and Frequency Control*, IEEE Transactions on , vol.56, no.5, pp.1074-1084, May 2009

[11] A. Bhuyan, J. W. Choe, B. C. Lee, I. Wygant, A. Nikoozadeh, O. Oralkan, B. T. Khuri-Yakub, “3D volumetric ultrasound imaging with a 3232 CMUT array integrated with front-end ICs using flip-chip bonding technology,” *IEEE Int. Solid-State Circuits Conf. (ISSCC) Dig. Tech. Papers*, pp. 396-397, Feb. 2013.

[12] R.J. Przybyla, H. Tang, Guedes, A.,S.E. Shelton, D.A. Horsley, B.E. Boser, ”3D Ultrasonic Rangefinder on a Chip,” in *Solid-State Circuits, IEEE Journal of* , vol.50, no.1, pp.320-334, Jan. 2015

[13] H. Tang, Y. Lu, S. Fung, J.M. Tsai, M. Daneman, D.A. Horsley, B.E. Boser, ”Pulse-echo ultrasonic fingerprint sensor on a chip,” in *Solid-State Sensors, Actuators and Microsystems (TRANSDUCERS)*, 2015 Transducers - 2015 18th International Conference on , vol., no., pp.674-677, 21-25 June 2015

[14] M. H. Abdul Halim, N. Buniyamin, M. A. Mohd Shari, R. Abu Kassim, Z. Mohamad, ”The use of ultrasound As a fat measurement sensor for the food industry: A review,” in *Smart Instrumentation, Measurement and Applications (ICSIMA)*, 2013 IEEE International Conference on, 2013, pp. 1-6.

[15] Texas Instrument,”Evaluation Board for the Ultrasound Transmit Solution,” http://www.ti.com/tool/tx-sdk-v2

[16] U.S. Food and Drug Administration. (n.d.). Retrieved November 20, 2015, from http://www.fda.gov/radiation-emittingproducts/ radiationemittingproductsand-procedures/medicalimaging/ucm115357.htm

[17] K. Chen, H-S Lee, A.P. Chandrakasan, C.G. Sodini, ”Ultrasonic Imaging Transceiver Design for CMUT: A Three-Level 30-Vpp Pulse-Shaping Pulser With Improved Efficiency and a Noise-Optimized Receiver,” in *Solid-State Circuits, IEEE Journal of*, vol.48, no.11, pp.2734-2745, Nov. 2013

[18] Texas Instrument, ”LM96550 8-Channel, Ultrasound Pulser with Active Clamp and Over Temperature Protection,” http://www.ti.com/product/lm96550

[19] A. Banuaji, H-K Cha, ”A 15-V Bidirectional Ultrasound Interface Analog Front-End IC for Medical Imaging Using Standard CMOS Technology,” in *Circuits and Systems II: Express Briefs, IEEE Transactions on*, vol.61, no.8, pp.604-608, Aug. 2014

[20] H-. Y. Tang, Y. Lu, S. Fung, D. A. Horsley, B. E. Boser, “Integrated ultrasonic system for measuring body-fat composition,” *IEEE Int. Solid-State Circuits Conf. (ISSCC) Dig. Tech. Papers*, pp. 22-26, Feb. 2015.

[21] M. Khorasani, L. van den Berg, P. Marshall, M. Zargham, V. Gaudet, D. Elliott, S. Martel, “Low-power static and dynamic high-voltage CMOS level-shifter circuits,” Dig. Int. Conf. Circuits and Systems (ISCAS), pp. 1946-1949, May 2008.

[22] Y. Moghe, T. Lehmann, T. Piessens, "Nanosecond delay floating high voltage level shifters in a 0.35 μm HV-CMOS technology," *IEEE J. Solid-State Circuits*, vol. 46, no. 2, pp. 485-497, Feb. 2011.

[23] C.Q. Tran, H.Kawaguchi, T. Sakurai, "Low-power high-speed level shifter design for block-level dynamic voltage scaling environment," in Integrated Circuit Design and Technology, 2005. ICICDT 2005. 2005 International Conference on , vol., no., pp.229-232, 9-11 May 2005

[24] M. D. Seeman, S. R. Sanders, "Analysis and optimization of switched-capacitor DC-DC converters," *IEEE Comp. in Power Elec.*, pp. 216-224, Jul. 2006.

[25] Senturia, S. (2002). Microsystem Design. Boston, MA: Springer US.

[26] Ultrasim. (n.d.). Retrieved November 21, 2015, from http://www.mn.uio.no/ifi/english/research/groups/dsb/resources/software /ultrasim/index.html

[27] G.S. Kino. Acoustic Waves: Devices, Imaging, and Analog Signal Processing, 1st ed. Englewood Cliffs, NJ, USA: Prentice-Hall, 1987.

[28] T.L. Szabo. Diagnostic Ultrasound Imaging: Inside Out. Burlington, MA, USA: Elsevier Academic Press. 2004.

[29] D. Seo, H-. Y. Tang, J. M. Carmena, J. M. Rabaey, E. Alon, B. E. Boser, M. M. Maharbiz, "Ultrasonic beamforming system for interrogating multiple implantable sensors," *IEEE EMBC*, Aug. 2015.

[30] Fingerprints, "FPC1011F3", http://www.fingerprints.com/wp-content/uploads/2014/01/FPC1011F3_product-sheet.pdf

[31] H. Plotnick, H. Pinkus, "The epidermal vs. the dermal fingerprint: an experimental and anatomical study", in *AMA archives of dermatology*, 1958, 77.1: 12-17.

[32] S. E. Gammal *et al*, "Sonography of the skin at 100 MHz enables in vivo visualization of the stratum corneum and viable epidermis in palmar skin and psoriatic plaques" in *J Invest Dermatol 1999*; 113: 8219.

[33] A. Maeva, F. Severin, "High resolution ultrasonic method for 3D fingerprint recognizable characteristics in biometrics identification," *Ultrasonics Symposium (IUS)*, pp.2260-2263, Sept. 2009

[34] R. M. Schmitt *et al.*, "Ultrasonic imaging of fingerprints using acoustical impediography," *Ultrasonics Symposium*, 2004 IEEE, 2004, pp. 680-688 Vol.1.

[35] A. Savoia, G. Caliano, A. Iula, C. Longo, A. Caronti, R. Carotenuto, M. Pappalardo,"Design and fabrication of a cMUT probe for ultrasound imaging of fingerprints," *Ultrasonics Symposium (IUS)*, 2010 IEEE, vol., no., pp.1877,1880, 11-14 Oct. 2010

[36] H. Y. Tang *et al.*, "11.2 3D ultrasonic fingerprint sensor-on-a-chip," *2016 IEEE International Solid-State Circuits Conference (ISSCC)*, San Francisco, CA, USA, 2016, pp. 202-203.

[37] "Peer Reviewed Glossary of the Scientific Working Group on Friction Ridge Analysis, Study and Technology (SWGFAST)" (PDF).http://www.swgfast.org/documents/glossary/090508_ Glossary_ 2.0.pdf, Retrieved 2016-03-22.

[38] "Layers of epidermis" (PNG). https://www.studyblue.com/notes/note/n/tissues-exam/deck/14916781, Retrived 2016-03-22.

[39] J. M. Cannata, T. A. Ritter, Wo-Hsing Chen, R. H. Silverman and K. K. Shung, "Design of efficient, broadband single-element (20-80 MHz) ultrasonic transducers for medical imaging applications," in *IEEE Transactions on Ultrasonics, Ferroelectrics, and Frequency Control*, vol. 50, no. 11, pp. 1548-1557, Nov. 2003.

[40] X. Jiang *et al.*, "Monolithic 591×438 DPI ultrasonic fingerprint sensor," *2016 IEEE 29th International Conference on Micro Electro Mechanical Systems (MEMS),* Shanghai, China, 2016, pp. 107-110.

[41] "Sylgard 184 silicone elastomer kit", http://www.dowcorning.com /applications/search/products/Details.aspx?prod=01064291, retrieved 2016-03-22.

[42] Analog Devices, "AD9212", http://www.analog.com/media/en/technical-documentation/data-sheets/AD9212.pdf, retrieved 2016-04-04.

[43] J. M. Tsai *et al.*, "Versatile CMOS-MEMS integrated piezoelectric platform," Solid-State Sensors, Actuators and Microsystems (TRANSDUCERS), 2015 Transducers - 2015 18th International Conference on, Anchorage, AK, 2015, pp. 2248-2251.

[44] Opal Kelly, "XEM6010-LX45", https://www.opalkelly.com/products/xem6010/, retrieved 2016-04-04.

[45] H. Tang *et al.*, "Pulse-echo ultrasonic fingerprint sensor on a chip," *Solid-State Sensors, Actuators and Microsystems (TRANSDUCERS), 2015 Transducers - 2015 18th International Conference on*, Anchorage, AK, 2015, pp. 674-677.

[46] R.J. Przybyla, S.E. Shelton, A. Guedes, I.I. Izyumin, M.H. Kline,D.A. Horsley, B.E. Boser, "In-Air Rangefinding With an AlN Piezoelectric Micromachined Ultrasound Transducer," *Sensors Journal, IEEE,* vol.11, no.11, pp.2690,2697, Nov. 2011

[47] R. J. Przybyla, H. Y. Tang, A. Guedes, S. E. Shelton, D. A. Horsley and B. E. Boser, "3D Ultrasonic Rangefinder on a Chip," in *IEEE Journal of Solid-State Circuits,* vol. 50, no. 1, pp. 320-334, Jan. 2015.

[48] National Institute of Standards and Technology, http://www.nist.gov, retrieved 2016-03-22.

[49] M. I. Skolnik, Introduction to Radar Systems. Boston, MA, USA: McGraw Hill, 2001.

[50] F. M. Rotella, G. Ma, Z. Yu and R. W. Dutton, "Modeling, analysis, and design of RF LDMOS devices using harmonic-balance device simulation," in *IEEE Transactions on Microwave Theory and Techniques,* vol. 48, no. 6, pp. 991-999, Jun 2000.

[51] Y. Moghe, T. Lehmann, T. Piessens, Nanosecond delay floating high voltage level shifters in a 0.35 μm HV-CMOS technology, *IEEE J. Solid-State Circuits*, vol. 46, no. 2, pp. 485-497, Feb. 2011.

[52] H. Y. Tang *et al.*, "Miniaturizing Ultrasonic System for Portable Health Care and Fitness," in *IEEE Transactions on Biomedical Circuits and Systems*, vol. 9, no. 6, pp. 767-776, Dec. 2015.

[53] D. Bianchi, F. Quaglia, A. Mazzanti and F. Svelto, "A 90Vpp 720MHz GBW linear power amplifier for ultrasound imaging transmitters in BCD6-SOI," *Solid-State Circuits Conference Digest of Technical Papers (ISSCC)*, 2012 IEEE International, San Francisco, CA, 2012, pp. 370-372.

[54] K. Chen, H. S. Lee, A. P. Chandrakasan and C. G. Sodini, "Ultrasonic Imaging Transceiver Design for CMUT: A Three-Level 30-Vpp Pulse-Shaping Pulser With Improved Efficiency and a Noise-Optimized Receiver," in *IEEE Journal of Solid-State Circuits*, vol. 48, no. 11, pp. 2734-2745, Nov. 2013.

[55] D. C. Daly and A. P. Chandrakasan, "An Energy-Efficient OOK Transceiver for Wireless Sensor Networks," in IEEE Journal of Solid-State Circuits, vol. 42, no. 5, pp. 1003-1011, May 2007.

[56] T. Shimamura, *et al.*, A Fingerprint Sensor with Impedance Sensing for Fraud Detection, *ISSCC Dig. Tech. Papers,* pp.170-171, Feb. 2008.

[57] Vandrico. (2014). *Wearable tech market* [Online]. Available: http://vandrico.com/wearables

[58] J. Seo, S. J. Pietrangelo, H. S. Lee and C. G. Sodini, "Carotid arterial blood pressure waveform monitoring using a portable ultrasound system," Engineering in Medicine and Biology Society (EMBC), 2015 37th Annual International Conference of the IEEE, Milan, 2015, pp. 5692-5695.

[59] D. Seo, et al. "Neural dust: An ultrasonic, low power solution for chronic brain-machine interfaces." arXiv preprint arXiv:1307.2196 (2013).